Università degli Studi di Padova

DIPARTIMENTO DI DIPARTIMENTO DI FISICA E ASTRONOMIA GALILEO GALILEI

Corso di Laurea magistrale in Astronomia

MASTER THESIS

Helium and multiple stellar populations in the massive outer-halo globular cluster NGC 2419

Candidato:
Marco Zennaro

Relatore:
Prof. Antonino Milone

Correlatore:
Dott.essa Anna F. Marino

Anno Accademico 2018-2019

Thesis advisor: Professor Antonino Milone, Anna Marino   Marco Zennaro

Helium and multiple stellar populations in the massive outer-halo globular cluster NGC 2419

Abstract

Recent work revealed that both the helium variation within globular clusters (GCs) and the relative numbers of first and second-generation stars (1G, 2G) depend on the mass of the host cluster. Precise determination of the internal helium variations and of the fraction of 1G stars are crucial constraints to the formation scenarios of multiple populations (MPs). We exploit multi-band Hubble Space Telescope photometry to investigate MPs in NGC2419, which is one of the most-massive and distant GCs of the Galaxy, almost isolated from its tidal influence. We find that the 1G hosts the $\sim 37\%$ of the analyzed stars, and identified three populations of 2G stars, namely 2GA, 2GB, and 2GC, which comprise the $\sim 20\%$, $\sim 31\%$ and 12% of stars, respectively. We compare the observed colors of these four populations with the colors derived from appropriate synthetic spectra to infer the relative helium abundances. We find that 2GA, 2GB, and 2GC stars are enhanced in helium mass fraction by $\delta Y \sim 0.01$, 0.06, and 0.19 with respect to 1G stars that have primordial helium (Y=0.246). The high He enrichment of 2GC stars is hardly reconcilable with most of the current scenarios for MPs. Furthermore, the relatively larger fraction of 1G stars ($\sim 37\%$) compared to other massive GCs is noticeable. By exploiting literature results, we find that the fractions of 1G stars of GCs with large perigalactic distance are typically higher than in the other GCs with similar masses. This suggests that NGC2419, similarly to other distant GCs, lost a lower fraction of 1G stars.

iii

Contents

Acknowledgments

1

Introduction

*

Globular clusters (GCs) are among the oldest systems in our Galaxy and among the most studied objects in the universe. However, we still struggle in understanding how they formed and why they are so common around every kind of galaxies, from giant elliptical

---

*This chapter is based on the reviews by Bastian & Lardo 2018[5] and Renzini et al. 2015[52]

galaxies to dwarf galaxies.

GCs present themselves as collections of stars, with a density above that of the stellar field, held together by mutual gravitational attraction and orbiting a galactic core. They are usually populated by around ten thousands to more than hundreds of thousands of stars, highly spherical in shape and are found more frequently in the galactic bulges and halos.

These clusters were for long thought as perfect examples of simple stellar population (SSP) systems, meaning a set of stars of the same age and initial chemical composition (in terms of both He and metal abundances) and different mass, distributed according to an initial mass function (IMF). A SSP is depicted by a single isochrone, which is a model representing how a population of stars of the same age and chemical content distribute on a color magnitude diagram (CMD), i.e. a plot having the clusters' stars colour[†] in the abscissa and their magnitude in the ordinate. The CMD of the globular cluster NGC6397 (from Anderson et al. 2008[8] and Bedin et al. 2009[3]) is shown in the left panel of Fig.1.1, while in the right panel an isochrone (represented in red) is over imposed on the same CMD. From what is shown the fit appears well done as there are no big differences between the line and the shape of the CMD.

Following this belief many concepts of stellar evolution theories were modelled in order to reproduce the same star dispositions in the CMDs observed in clusters.

1.1   Multiple Stellar Populations in Globular Clusters

However not everything was as ideal as it seemed. In the early seventies chemical inhomogeneities among bright giants in clusters were discovered (Osborn 1971)[50]. Furthermore

---

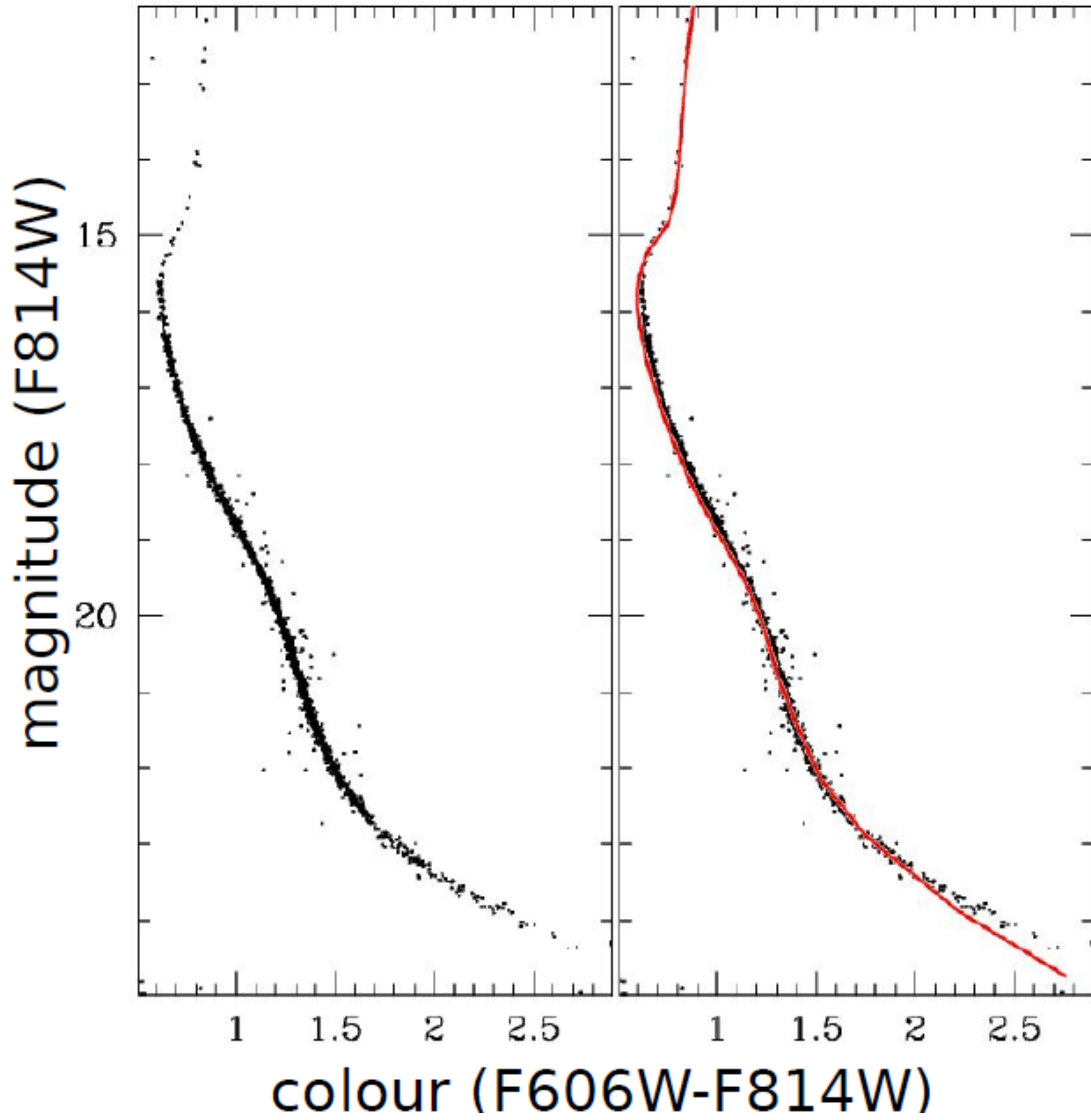[†]A star colour is its magnitude difference in two distinct filters

Figure 1.1: In the right panel is shown an example of the fitting of an isochrone (red line) over the CMD of NGC 6397 shown in the left panel. At a first glance the approximation to a SSP seems really good, i.e. the star distribution is close to the isochrone. From Bedin et al. (2009)[8] and Anderson et al. (2008)[3].

Bell and Dickens (1980)[9] found that stars with the same magnitude in the red giant branch (RGB) of the CMD showed variations in the strengths of CH, CN, and NH blue absorption features, due to intrinsic star-to-star variations in C and N abundances, in addition N was found to anti-correlate with C.

An explanation of these inhomogeneities was at first attempted through evolutionary mixing as normal stellar evolution may contribute to the observed N-C anti-correlation in evolved RGBs (Denisenkov & Denisenkova 1990)[23]. However this hypothesis was disproved when the same chemical variations were discovered in non, or scarcely, evolved main sequence (MS) or turn-off (TO) star (Cannon et al. 1998[12]).

Moreover, when higher resolution spectra became available, it was possible to measure Na and O abundances in stars with already measured N and C ones. From these measurements it was found that a nitrogen overabundance was correlated with enhanced sodium, while carbon depletion was correlated with decreased oxygen (Sneden et al. 1992[55]).

Another key feature of multipopulations in GCs is the helium variation. Observational data suggest a correlation between N variations and He enhancement. While it is difficult to obtain direct spectroscopic determinations of the helium variations, they can be estimated by assuming that the observed colour dispersions at a given magnitude on the MS in optical colours are primarily due to He spreads. Recent studies (Milone 2015[43]), using HST photometry found that He spreads correlate with the cluster mass and luminosity, with more massive and luminous clusters showing larger spreads.

These evidences hinted that globular clusters are composed not by a SSP but by multiple stellar populations (MSPs or MPs) given by a sum of different single 'generations' each one with its own chemical composition. It is usual to refer to the stars with a primordial chem-

4

ical composition as 'first generation' (1G) or 'first population' (1P), and to he enriched ones as 'second generation' (2G) or 'second population' (2P).

These different populations are commonly observed through accurate photometry in appropriate filters. They appear in CMDs of clusters as split or spread sequences that have been used to identify MSPs and their characteristics. These split and spread sequences are generated by the different chemical composition and revealed through the colours (or colours combination) used to obtain the CMD. Filters in wavelengths shorter than ~ 4000 Åare very sensitive to variations of C, N and O in the outer layers of stars with cooler atmospheres, while the combination of optical and UV bands is useful to reveal He variations as they impact the stellar structure.

MS and RGB stars with different helium abundance but the same luminosity have different effective temperature. As a consequence, CMDs with wide color baselines are efficient tools to identify helium variations within GCs. C and N variations mostly affect the ultraviolet region of the spectrum. For this reason, multiple or spread sequences are visibile in photometric diagrams made with appropriate combinations of UV and near-UV filters. It is useful, to better examine these aforementioned features, to introduce colour indexes suitable to analyze the MPs in GCs (e.g. with the HST WFC3/UVIS filters F275W, F336W and F438W $C_{F275W,F336W,F438W}$ can be constructed as $(F275W - F336W) - (F336W - F438W)$) as those represented in fig.1.2.

Another powerful instrument to distinguish different populations in GCs are the so-called chromosome maps. Chromosome maps are diagrams with a colour as the abscissa and a colour index as the ordinate (fig 1.3). In these plots stars of different populations, i.e. with different chemical compositions, tend to clump together and it is easy to separate be-
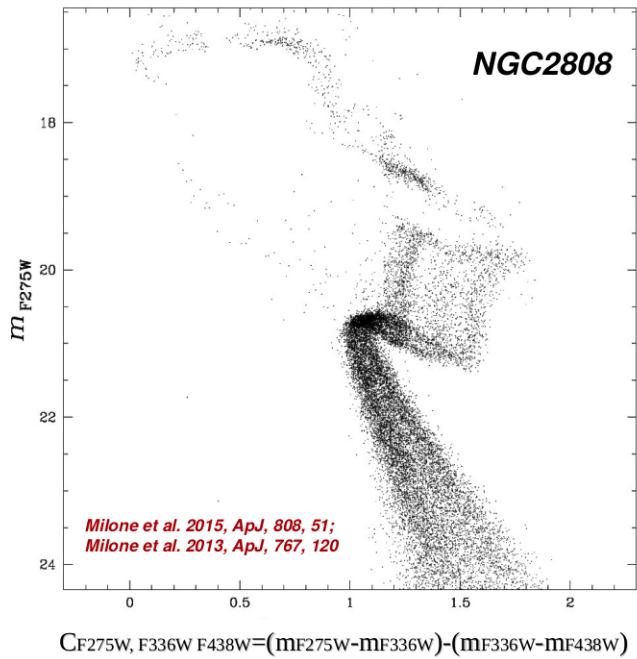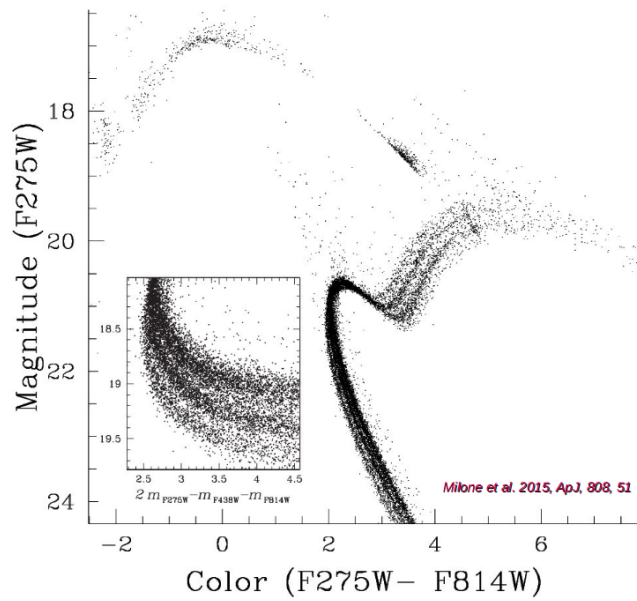
Figure 1.2: On the lower is the pseudo colour $C_{F275W,F336W,F438W}$ vs the magnitude in the filter F275W, while on the upper is a 'normal' CMD but built using the F275W-F814W filter combination. Using these tools we can see features, such as splittings or enlarged widths, in the RGB which were not visible in the normal CMD in Fig.1.1 (From Milone et al. 2013,2015)
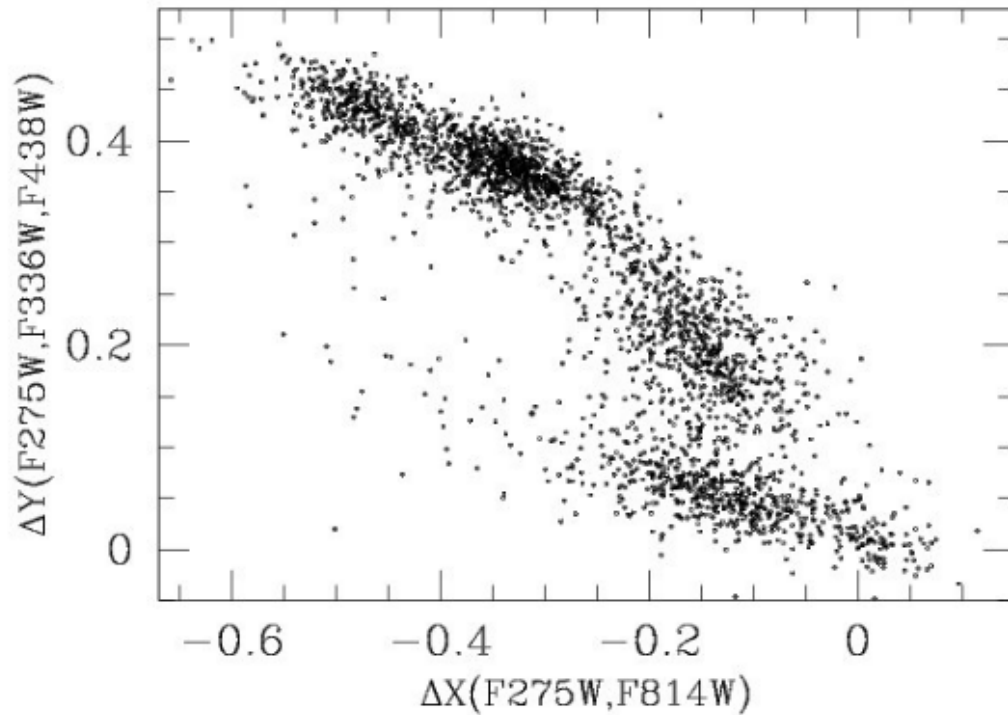
Figure 1.3: Chromosome map of RGB stars of NGC 2808, the same cluster of Fig.1.2. It is clear the power of the so-called chromosome maps to separate the different populations with respect to a normal CMD. From Milone et al. (2015).

tween the multiple populations of a cluster. With such diagrams, Milone et al. (2017)[47] were able to efficiently distinguish the 1P and 2P populations for a sample of 58 GCs. These distinctions were confirmed through comparison with the results of ground based spectroscopic studies, i.e. 1P stars identified photometrically corresponded to stars with the field abundance patterns of Na and O (e.g. Marino et al., 2019, submitted to MNRAS).

RELATIONS WITH CLUSTER PROPERTIES

MPS AND CLUSTER MASS   Milone (2015)[43] found that the helium spreads (ΔY) within galactic GCs are higher in more massive clusters. This was confirmed in 2017 by Milone et

al.[47] who measured He variations from a larger cluster sample of the UV GC Legacy Survey. Milone and collaborators also found that the width of the RGB of those clusters, in the (F275W-F814W) CMD, is correlated with the He internal spreads.

This finding suggests that more massive clusters, with deeper gravitational potential well, could have been capable to sustain more complex or prolonged star formation. Higher mass clusters also shows larger spreads of Na-O abundances (e.g. Carretta et al. 2010[13]; Marino et al. 2019, subs. to MNRAS) Another quantity that was found to relate with the cluster mass, in the context of the UV GC Legacy Survey by Milone et al. (2017)[47], is the fraction of enriched stars $f_{enriched}$ with higher mass clusters (e.g.$\sim$ $10^6 M_\odot$) having $f_{enriched} \approx 0.8$ and clusters with masses near $10^5 M_\odot$ having $f_{enriched} \sim 0.4 \sim 0.5$.

1.2   Theories on MSP formation

All theories on the formation of the multiple population in globular clusters must obey the observational constraints, which we can summarize as in Renzini et al. (2015)[52]:

- GC specificity. The presence of second generation stars in globular clusters is very common while they are rare in the Milky Way field. Their small number in the field is consistent with them having been generated within GCs and then lost by them through tidal interactions.

- Ubiquity. 2G stars are found in almost all the studied GCs. This hints that the appearance of this type of stars is probably an outcome of the formation process of GCs.

- Variety. While multiple populations are present in almost any globular cluster, each

one of them has its own specific pattern, i.e. no two cluster show the same exact composition.

- Predominance. Second generation stars are not a minority of the stars in a cluster, rather they can even dominate.

- Discreteness. Every population is quite distinguishable in appropriate two colours or colour magnitude diagrams.

- Supernova avoidance. In most GCs the 2G stars share the same metallicity of the 1G stars, thus they experienced very little to no contamination by supernova products.

- Hot CNO and NeNa processing. A distinctive characteristic of 2G stars is the chemical composition that results from CNO-cycling and p-capture processes at high temperatures.

- Helium enrichment. Proofs of He enrichment have been found in 2G stars in every cluster studied.

- Mass budget. As said before 2G stars are dominant in GCs. This means that if only a fraction of the initial 1G mass is transferred to them it must be explained where the required mass to form 2G stars comes from.

There are several different theories and scenarios that try to explain the existence of MSPs, in the following subsection I will present the most popular ones and try to compare them with the constraints mentioned above.

1.2.1 SUPERMASSIVE STARS

In this model, proposed by Denissenkov & Hartwick (2014)[24] and Denissenkov et al. (2015)[25], it is proposed that the most massive stars within a young GC, because of dynamical friction, will move towards its center. There they give birth to super massive stars (SMS) of $\sim 10^4 M_\odot$. These SMSs, for this model, would be fully convective and with a luminosity close, or exceeding, the Eddington limit, meaning they would loose mass at a high rate. As the SMS evolve, since they are fully convective and thus can be considered chemically homogeneous, their wind would be progressively enriched in He, CNO-cycle and p-capture products as requested by the mentioned observational constraints.

In this scenario the requirement of GC specificity is met since its parameters are fundamental in the SMS formation. Variety may be expected, e.g., from different possible masses of the SMS and from different timing of the 2G star formation. Discreteness of the multiple populations may be accommodated appealing to separate bursts of star formation taking place at different stages of pollution of the inter stellar medium (ISM) by the SMSs.

A difficult constraint to reconcile with this theory is the supernova avoidance because both 2G and supermassive stars have to form before the first massive stars turn into supernovae. In this scenario the SMS should be in a very strict mass range around $10^4 M_\odot$ otherwise they would not produce the required quantity of p-capture elements and it is predicted that such stars should fragment and fall apart once helium is increased to Y=0.4, making this the upper limit of He for 2G stars. Thus, to test this prediction it is interesting to compute accurately the He enrichment in clusters that seem to have extreme helium variations as NGC 2419 does ($\Delta Y \sim 0.17 - 0.19$ from Di Criscienzo et al. (2011)[28] and Lee et al. (2013)[38]). Another problem of this model is the mass budget: the limit imposed to the mass

of the SMS makes it impossible for them to deliver the required amount of helium.

1.2.2 Fast rotating massive stars

According to the fast rotating massive stars (FRMSs) scenario (as proposed by Krause et al. 2013[35]) the enriching materials are produced in the interiors of massive stars ($\sim 20 - 100 M_\odot$) with high rotational velocities. High rotational velocities are needed because these stars, unlike SMSs, are not fully convective. Thus the mixing agent is the fast rotation: it brings the nuclear burning products to the envelope from which they expelled in the ISM.

This process, however, is not specific to globular clusters, as it involves all FRMSs, so we should find stars with the same chemical patterns of 2G stars even in the galactic halo field which are not observed. Furthermore given the star-by-star formation process, one may expect little variation from one batch of 2G stars to another, as 2Gs would arise from the contribution of very many FRMSs. Even the discreteness of 2G populations requirement is difficult in this theory, as this method of formation would create continuous distribution of abundances.

Supernova avoidance is also a major problem. The fast winds from massive stars, and from their supernova explosions, make the extremely crowded central regions of GCs too harsh of an environment to avoid contamination by supernova products or even for them to survive at all. The mass budget and detailed abundances of 2Gs are also a problem for this scenario.

1.2.3 Massive interactive binaries

In the massive interactive binaries (MIBs) scenario (de Mink et al. 2009[21], Bastian et al. 2013[4]), the forced rotation of the primary envelope would cause mixing. If this mixing reaches the hydrogen-burning shell it leads to a processing of the envelope by the CNO-cycle and p-capture hence producing helium enhancement, oxygen depletion, etc. Then the envelope, after a common envelope phase of the MIB, is shed in the ISM. MIB ejecta would then be be swept up by the circumstellar disks of young, low-mass stars and eventually dumped onto the stars themselves.

This scenario is certainly cluster specific, as only in a dense enviroment like in GCs high densities in the ISM can be reached which are necessary for appreciable accretion to take place, and even the variety requirement can be met. However the discreteness constraint is not, as even in this case the expected abundance variations in 2G stars are continuous. Supernova avoidance is another problem, as 1G MIBs would inevitably coexist the supernovae from single stars as well as from MIBs themselves that too would pollute the ISM.

1.2.4 AGB stars

AGB stars have been proposed as a possible of origin of both the abundance spreads (D'Antona, Gratton & Chieffi 1983[19]; Renzini 1983[51]; Iben & Renzini 1984[33]) and the composition patterns of populations in GCs (D'Ercole et al. 2010[26]). During their AGB phase stars in the mass range of $\sim 3 M_\odot$ to $\sim 8 M_\odot$ experience the hot bottom burning (HBB) phenomenon, during which, at bottom of the envelope, high temperatures are reached and p-capture nuclear processing is made possible. Below this $3 M_\odot$ threshold stars do not experience the HBB, thus the AGB is populated by carbon stars. Since these type of stars are not found

among 2Gs it is implied that in this scenario the formation this second generation stars must be concluded before $3\mathcal{M}_\odot$ stars enter the AGB phase.

DErcole et al (2010)[26] proposed a version of this model in which a massive GC progenitor has a major episode of star formation leading to the birth of the first generation, the residual gas is then blown away by supernova explosions. After the supernova era AGB stars begin to eject their enriched materials, and since their ejection velocity is lower than the escape velocity, they accumulate within the potential well of the system. A cooling flow is then established, leading to accumulation of gas within the original nucleus, until one or more star bursts make the 2G stars. The GC will then evolve on account of the tidal interaction with the parent galaxy, this interaction will strip the GC of most of its 1G stars leaving it with a comparable fraction of 1G and 2G stars. To investigate this particular prediction it is of extreme interest to study very distant and isolated GCs like NGC 2419 analyzed in this work.

In this model the composition of the ISM is rapidly changing in the AGB phase, thus every star burst leads to 2G stars with different characteristics and that will meet the discreetness constraint. Variety is explained since every GCs will have its own star formation history (SFH). Since the 2G SFH happens after the 1G supernova era, the supernova avoidance is automatically fulfilled at least from 1G stars, but if there is more than one 2G star burst, supernovae from stars of the first 2G burst may contaminate the later generations which would be a problem as this contamination is not found by the observations.

Furthermore this scenario does not produce a Na-O anti-correlation, but rather a correlation. In order to reproduce the anti-correlations a re-accretion of pristine material is required, but there is no solid explanation to where this material would have been stored

and and how did it avoid being contaminated by 1G supernovae.

The mass budget constraint is explained by considering a sufficiently massive precursors, however it is still not perfectly clear how much massive it must be.

1.3 Thesis layout

In this work I will study the globular cluster NGC2419. This cluster is particularly interesting because it is one of the most-massive and distant GCs of the Galaxy, almost isolated from its tidal influence, thus we would expect that it has retained its initial mass and the fraction of 1G stars. I will use the same methods used by Milone et al. (2017, 2018) in order to investigate multiple stellar populations in NGC2419. The rest of the thesis in organized as follows: In Chapter 2 I present the data and the data reduction. The data analysis is described in Chapter 3, while results are presented in Chapter 4 where I also provide some discussion and conclusion.

2

Data and data reduction

To investigate the multiple stellar populations of NGC2419 I used archive images, in 14 different filters of the Ultraviolet and Visual Channel of the Wide Field Camera 3 (UVIS/WFC3) on board of HST. These data were collected from two separate programs: filters F225W, F275W F300X, F390W, F438W, F475x & W, F555W, F606W, F625W, F775W and F814W from the GO11903 program, with J. Kalirai as its PI, with the main purpose of improving
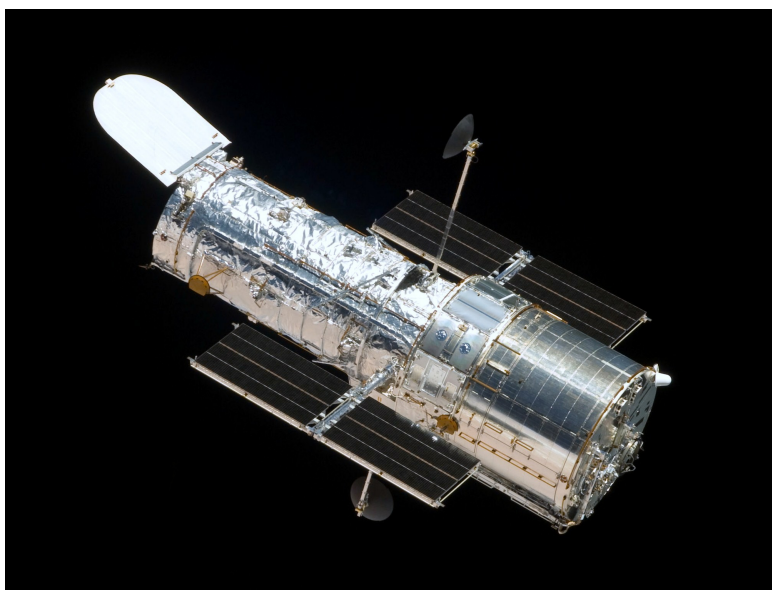
Figure 2.1: Image of the Hubble Space Telescope taken from the space shuttle Atlantis.

the UVIS photometric zero points while filters F336W and F343N from the GO15078, PI S. Larsen which is a project focused on the dynamics of multiple populations in NGC2419. In this chapter I give a brief description of the HST telescope, used to retrieve the data, and of NGC 2419, subsequently I describe the procedure and programs used in the reduction process,

2.1 HUBBLE SPACE TELESCOPE

Before describing the process used to analyze the data, I want to dedicate a section to the Hubble Space Telescope (HST) (Fig.2.1). Launched in 1990 the HST has become one of the most, if not the most, well-known astronomical instrument ever built and without any doubts the incredible images produced have contributed to its fame.

Built by the United States space agency NASA, with contributions from the European

Space Agency, the HST is a Cassegrain reflector of Ritchey–Chrétien design, meaning it has a hyperbolic primary mirror and a hyperbolic secondary mirror. The primary mirror has a diameter of 2.4 meters and weights 828 kilograms while the secondary measures 0.30 m and weights 12.3 kg. These numbers might not seem enormous, specially if compared to the modern earth-based telescopes (e.g. the 40 m diameter of ESA's extremely large telescope), however the HST, being into space is not affected by the many distortions induced by the atmosphere thus is able to take extremely high-resolution images, with substantially lower background light than ground-based telescopes allowing it to probe deeper into our Universe than any telescope before it.

Another advantage of being outside the atmosphere, for the study of MSPs, is that the HST is sensible to wavelengths that are inaccessible from Earth observations, like for example the UV band $(\lambda = 10 - 400) nm$ which, as said in in sect. 1.2, is fundamental to discover and characterize the different stellar populations.

Thus it is not surprising if it was through the HST that it was possible to discover multiple stellar populations in several Galactic and extra-galactic globular clusters, as the Hubble Space Telescope is the only telescope that makes it possible to derive accurate measurements of fluxes and positions in those crowded environments.

On board of the HST, observing in the ultraviolet, visible and near infrared frequencies, there are currently six different instruments:

- Advance Camera for Survey (ACS) which has three independent, high-resolution channels: the Wide Field Channel (WFC), the High Resolution Channel (HRC) and the Solar Blind Channel (SBC). Together they cover the ultraviolet to the near-infrared regions of the spectrum.

- Cosmic Origins Spectrograph (COS) designed for ultraviolet (90–320 nm) spectroscopy of faint point sources with a resolving power ($\lambda/\Delta\lambda$) of about 1,550–24,000.

- Wide Field Camera 3 (WFC3) which is the camera used to collect the images I used in this work. The WFC3 has two channels, one for near infrared imaging (IR channel), and the UVIS channel operating between 2000 and 11000 Å.

- Near Infrared Camera and Multi Object Spectrometer (NICMOS). Now hiberating, it was noted for its performance in Near-infrared space astronomy, in particular its ability to see objects through dust.

- Space Telescope Imaging Spectrograph (STIS) which is, as the name says, a spectrograph but it also has a camera mode. The spectrograph has made many important observations, including the first spectrum of the atmosphere of an extra solar planet, (David K. Sing et al. 2008).

- The Fine Guidance Sensors (FGS) that provides high-precision pointing information as input to the observatory's attitude control systems.

2.2 NGC 2419

Discovered by William Herschel the 31st of December 1788[*], NGC 2419, shown in Fig.2.2 is a globular cluster in the Lynx constellation. It is nicknamed 'The Intergalactic Wanderer' as it was thought, erroneously, that this GC did not orbit around the MW. This mistake was due to its rather large distance to the center of our galaxy which is $d \sim 87.5 kpc$ (Di Criscienzo et al. 2011[28]) making almost isolated from the tidal influence of the Milky

---

[*] as reported by http://www.messier.seds.org/xtra/ngc/n2419.html

Figure 2.2: NGC 2419 'The Intergalactic Wanderer' as photographed by HST during the GO 11903 proposal.

Way. NGC 2419 is one of the most massive and metal poor globular cluster of our galaxy at $9x10^5 M_\odot$ and $[Fe/H] = -2.09$ (McLaughlin and van der Marel 2005[42]; Mucciarelli et al. 2012[48]).

Moreover, since its half-light relaxation time exceeds the Hubble time (Harris 1996), it would retain fossil information on the properties of multiple populations at the formation. The possibility that NGC2419 evolved in isolation, together with its extreme mass and metallicity, makes this cluster an ideal target to constrain the formation scenarios of multiple populations.

As said in sect. 1.3 in some theories on the formation of MSPs, to solve the problem of the mass budget, mentioned therein, speculate that GCs lose, due to tidal interaction with the galaxy, a considerable fraction of their 1G star. Thus those theories predict that a cluster that formed and evolved in isolation would retain its initial mass and the fraction of 1G

stars (up to $\sim 90\%$ of the total) while displaying similar enrichment in He and light elements as other GCs.

Multiple stellar populations in NGC2419 have been widely investigated both spectroscopically and photometrically. Based on high-precision photometry obtained from Wide Field Channel of the Advanced Camera for Survey (WFC/ACS) on the Hubble Space Telescope (HST), Di Criscienzo et al. (2011)[29] and Lee et al. (2013)[38] found that the base of the red-giant branch (RGB) of NGC2419 exhibits a wide $m_{F475W} - m_{F814W}$ color broadening that is consistent with two stellar populations with an extreme helium difference of $\Delta Y \sim 0.17 - 0.19$. Spectroscopy revealed large star-to-star variation in magnesium and potassium, at variance with most GCs that have homogeneous [K/Fe] (Cohen et al 2011[16], 2012[17]; Mucciarelli et al. 2012[48]). Stars with different abundances of Mg and K exhibit different colors in the V vs. $u - V$ CMD (Beccari et al. 2013[7]), in close analogy with what is observed in nearly all the GCs where stars with different light-element abundance populate distinct sequences in CMDs made with ultraviolet filters (Marino et al. 2008[41], Yong et al. 2008[60]).

2.3 Data Reduction

The data set consists in archive images, in 14 different filters of the Ultraviolet and Visual Channel of the Wide Field Camera 3 (UVIS/WFC3) on board of HST. In table 2.1 I review the properties of the images that were used in this work. In order to obtain the photometry and astrometry I used the program *Kitchen Sink 2* developed by Jay Anderson, similar to the software described in Anderson et al (2008)[3] to reduce images taken with the Wide Field Channel of the Advanced Camera for Survey but is optimized to work with images

FILTER	DATE	N×EXPTIME	PROGRAM	PI
F225W	May 15 2010	750s	11903	J. Kalirai
F275W	May 15 2010	400s	11903	J. Kalirai
F300X	May 15 2010	467s	11903	J. Kalirai
F336W	Apr 26 2018	2 × 1392 + 4 × 1448s	15078	S. Larsen
F343N	Apr 28 2018 - May 01 2018	4 × 1392 + 8 × 1448s	15078	S. Larsen
F390W	May 15 2010	300s	11903	J. Kalirai
F438W	May 15 2010	2 × 725s	11903	J. Kalirai
F475X	May 15 2010	275s	11903	J. Kalirai
F475W	May 15 2010	465s	11903	J. Kalirai
F555W	May 15 2010	2 × 580s	11903	J. Kalirai
F606W	May 15 2010	2 × 400s	11903	J. Kalirai
F625W	May 15 2010	600s	11903	J. Kalirai
F775W	May 15 2010	2 × 750s	11903	J. Kalirai
F814W	May 15 2010	2 × 650s	11903	J. Kalirai

Table 2.1: Parameters of the UVIS/WFC3 images of NGC2419 used in this work.

collected with various detectors of HST, including UVIS/WFC3.

First of all, the images have been corrected for the poor charge transfer efficiency (CTE) using the programs written and provided by Anderson and Bedin (2010)[1]. The authors derived a model that reproduces the trails observed in a large sample of analyzed dark exposures. The software works inverting this model: from the observed pixel counts it finds the original ones.

The next step to proceed in the data reduction process is to get the effective point spread function (ePSF)

2.3.1 EFFECTIVE POINT SPREAD FUNCTION

The aim of the data reduction is to produce a catalog, for each filter, of the stars of the GC. In order to do so, since in HST images of globular clusters essentially all of the objects are

relatively isolated point-source stars, we need to retrieve from the images the position of each source (x, y) and its flux (f). These parameters are derived from the array of pixels that constitute the image of the star, and by using the PSF.

The PSF in CCDs (Charged Coupled Devices) is given by the convolution of the functions that are not directly observed: the instrumental PSF (iPSF), which describes the flux of a point source as a function of the offset from its center, and the pixel response function which tracks the sensitivity at each point in the pixel.

Anderson and King (2000)[2] developed an innovative solution to this problem based on the construction of the effective point-spread function and to bypass the lack of knowledge of the two functions mentioned before. This ePSF consist in a continuous function of $(\Delta x, \Delta y)$, offset from the center of the PSF, whose value at any point is the fraction of light of a point source that would fall in a pixel centered at that point. Then, instead of forcing this function into a purely analytical function, it is treated empirically and its value is tabulated in an array of points.

A major challenge in building accurate PSF models arises from the poorly-sampled images delivered by HST. Since HST is in space, it is not affected by seeing defects induced by the atmosphere like earth based telescopes, for which, the PSF is distributed on more pixels so that the Full Width at Half Maximum (FWHM), of the iPSF, is generally 2-3 pixel. The point-spread function formed by HST has a core that is about 50 mas wide, depending on the wavelength, which is comparable to the pixel size of the ACS/WFC channel; thus making most of the flux fall into the central pixels. This undersampling makes it possible that different PSF models fit the the pixel values correctly while giving different location for the peak, see Fig.2.3, leading to a PSF degeneracy and a so-called 'pixel-phase error'. To avoid
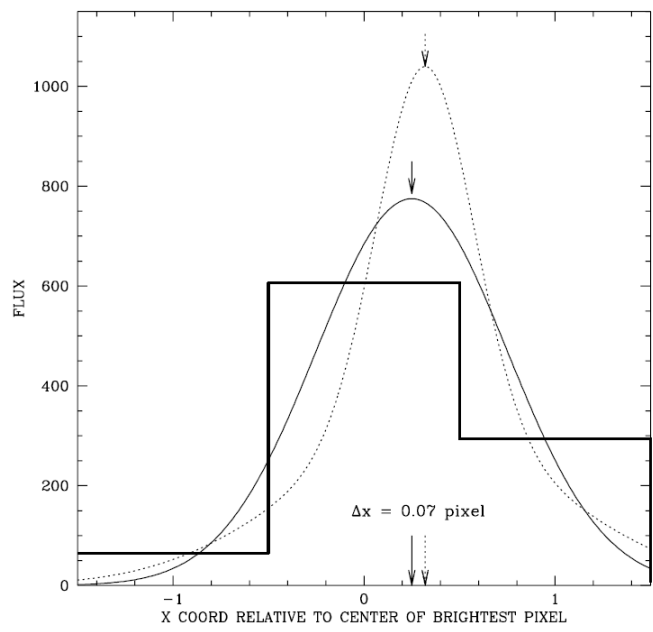
Figure 2.3: The histogram shows the pixel values for the innermost 3 pixels of an undersampled one-dimensional star profile. The solid curve is a pure Gaussian model which, when integrated over the pixels, fits their values exactly. The dotted curve is a composite of a sharper Gaussian with a small contribution from a broader one; integration over it also fits the pixels exactly. The arrows show the locations of the peaks of these two PSFs, which are offset by 0.07 pixel. From Anderson and King, 2000.
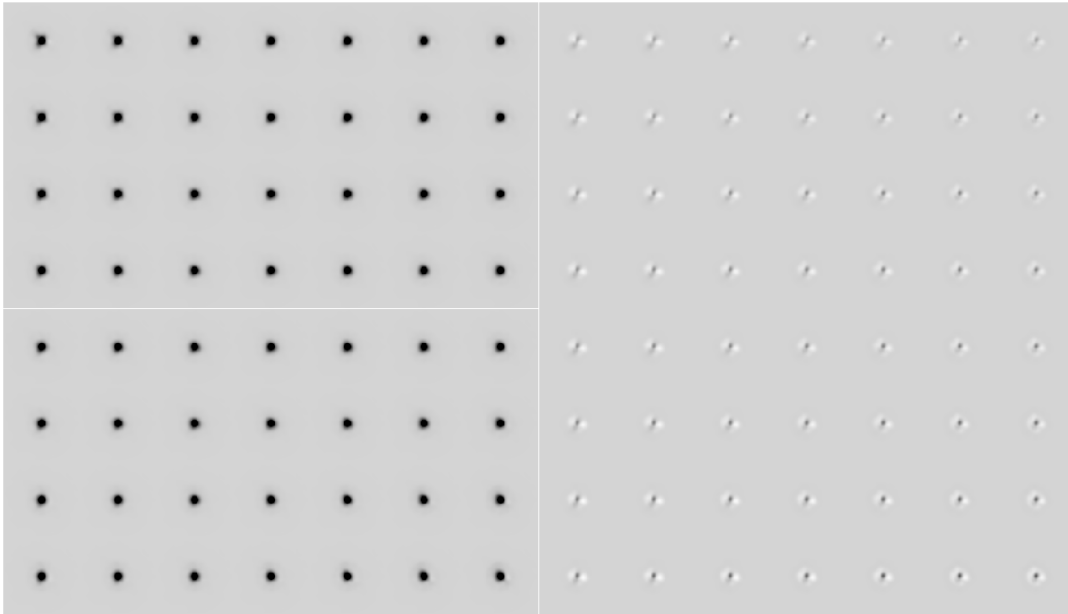
Figure 2.4: In this figure we can see an example of the grid of fiducial PSFs, in this case obtained in the F438W filter.

such problem the *dithering* technique is used. It consists of taking images slightly shifted, so that stars move from one image to another, breaking the degeneracy in the PSF model.

Another problem is that the PSF may change in shape depending on the location in the CCD, this is because of position depending charge diffusion and optical aberrations. To solve this issue and to derive the best possible PSF, i.e. the best possible astrometry and photometry, the fortran routines I used in this work account for spatial variations across the field of view. In order to do so instead of a single PSF the software computes a grid of fiducial PSFs, see Fig. 2.4. Then a PSF is built for any point in the detector simply interpolating the PSF among the four nearest grid points. In addition to spatial variability, PSF core changes over time with the change of focus, and this effect is called *breathing*. Since this time variability is decoupled from the spatial variability, we can represent the PSF as a

sum of a library PSF and a small perturbation PSF, built from the residuals of the fit of the star flux with the library PSF.

The situation, however, is somewhat different for the WFC3 camera that is the one used to get the images I utilized in this work, for this instrument the is 40 mas wide. Thus the resulting pictures are poorly sampled and not undersampled, still, the procedure I used in the data reduction process follows the same approach as the one explained above, see Sabbi et al. (2016)[53] and Bellini et al. (2017)[10] for more details. The software then follows two different methods to measure stars with different luminosities: for bright stars the magnitude and positions are measured in each exposure independently and then averaged, while for faint stars, in order to increase the signal to noise ratio, every image is stacked, combining the information from all the images image that are placed into a common distortion-free reference frame.

2.4 Reduction process

Determination of the PSF

The specific program I used in order to derive the PSF grids described in the previous section is *img2psf*, this software is used to compute extremely high accuracy ePSFs using the information from all the bright but not saturated and isolated stars from each exposure. *img2psf* starts with a pre computed library PSF, one for each different filter used for the images, and utilizes it as a starting guess to derive the aforementioned grid. In order to do so *img2psf* requests at least 7 arguments:

- Isolation index. It is used to select isolated stars, it states at which distance, from a

brighter pixel, a peak must be for it being considerate to calculate the PSF.

- Minimum flux. This argument specifies the the minimum value for a source to be considered in the determination of the PSF model. Since I wanted to select only bright stars I used FMIN=3000.

- Maximum flux. As opposite of the above, since saturated stars are not wanted in the construction process of the ePSF, it is the maximum flux value for a source for it to be considered. Since HST saturation happens at 55000 DNs I imposed FMAX=54999

- Maximum Q-fit. The Q-fit is a parameter which evaluates the quality of the fit, if the fit is perfect the q-fit will be 0 while the higher its value the worse the fit. This argument sets the maximum Q-fit value a star can have, after a fit with the library PSF, to be considered. I set QMAX=0.2 which excludes nearly all the non-stellar sources, like galaxies and cosmic rays and blended stars.

- Number of regions. Ranging from 1 to 5, it is the number of regions used to find the perturbation PSFs. The adopted value of NSIDES is the result of a compromise. Indeed, on one side, I would need a large number of regions to account for small-scale non-linear variations of the PSF across the chip. On the other hand, a small value of NSIDES would maximize the number of stars used in the PSF determination. I fixed a value of NSIDES=3 on the basis of the stellar density of each image. I verified that a larger value would result in a poor PSF model, due to small number of stars in each sub-region.

- Initial PSF guess. Meaning the library PSF used as a first guess.

- IMG.fits. Which is the image to analyze.

Photometry and astrometry of stars in the single images

With the correct ePSF built, the next step is to determine positions and fluxes of all the stars in the images by fitting to them the computed ePSF. This was done via the program *img2xym* (see Anderson and King, 2006 for details). This program takes as inputs parameters the isolation index, the minimum and maximum stellar fluxes, however, in this step, in contrast with the previous one, I wanted to include all stars, even saturated ones to be analyzed and fitted.

The output of this step is a text file with 4 columns in which are reported respectively for each star the values of: x, y, magnitude and q-fit. The first two refer to the coordinates in the reference frame of the image, the magnitude is in instrumental units, defined as

$$mag = -2.5 log(flux) \tag{2.1}$$

where the flux is expressed in photo-electrons recorded in the reference exposure, and the q-fit is indicative of the quality of the fit between the observed star and the best-model PSF.

To further proceed in the reduction, I needed to select only stars with relatively small values of the q-fit parameter which translates into stars for which is possible to do high precision photometry. This is required in order to discriminate between the effects of age and rotation in the cluster CMD and was done via a 'cleaning' process.

To perform the aforementioned 'cleaning' process, consisting in the selection of stars with high-precision photometry, firstly I divided all the stars in magnitude bins, with the bins size varying from image to image depending on the number of stars present, then, through a recursive iteration I computed the median q-fit and 68.27th percentile (σ). The recursive process was done as follows: after the computation of the median value each star exceeding 4 times the σ value is rejected and the median is re-evaluated and so on; the procedure is stopped when two subsequent measures of the median differ by less than the 1%. In the next step I added to the median value of each bin 5 to 6 times σ, (the exact number in this interval was chosen in order to draw the boundaries that follow the bulk of the distribution of each parameter value, see Fig. 2.5) In Fig.2.5 is represented the result of the 'cleaning' progress, the blue points are stars which were poorly fitted with the model PSF and thus discarded in the following steps. This procedure was repeated for every image in each filter.

The result of the 'cleaning' procedure is catalog containing the positions and magnitudes of the cluster stars for every image in each filter. However, since every image is different, every catalog has its own reference frame. Thus the next step is to find the right coordinate transformation from one to another and consequently creating a single reference catalog.

To find these coordinate transformation, the programs I used exploit the *cross identification* method, based on the fact that triangles do not change their basic shape (they remain similar) with translation, rotation, scale change or flip. To identify the shape each triangle, then, it is possible to utilize two independent and invariant shape parameters:
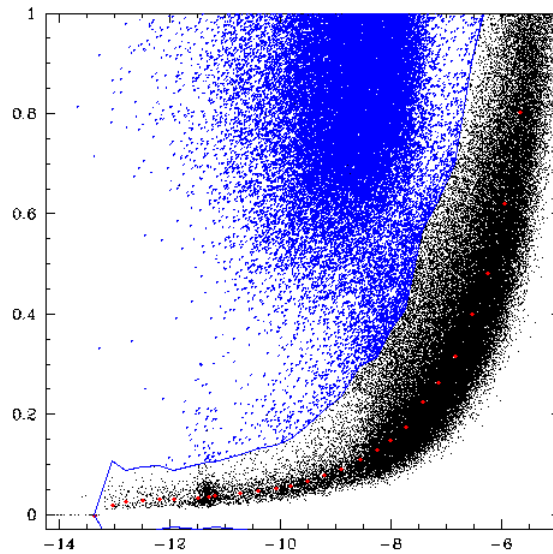
Figure 2.5: Result of the 'cleaning' process for one of the images (ibcd41caq_WJC) in the F438W filter. In the x-axis there are the instrumental magnitudes in the F438W filter, while in the y-axis are the q-fits of each star in the image. The red dots are the computed median values of the q-fit for each bin, and the blue line is the result of the interpolation. The blue points are the poorly fitted stars which were not included in the analysis.

- b/a. The ratio of the triangle's medium length side (b) to its longest (a).

- c/a. The ratio of the triangle's smallest length side (b) to its longest (a).

Therefore a triangle formed by three points (stars) in the CCD space, this can be identified by a point in a two-dimensional space (b/a, c/a), moreover, the same three stars will always form a triangle with the same shape in every image that will be represented by the same point in this space, independently from the transformations the stars suffer. Summarizing, firstly the program finds common stars, using the method mentioned above, and then it derives the parameters of the transformation. In the case of a combined rotation, translation, tilt and scale change there can be up to six different parameters describing the transforma-

29

tion:

$$
\begin{cases}
x_1 = A + C \cdot x_2 + E \cdot y_2 \\
y_1 = B + D \cdot x_2 + F \cdot y_2
\end{cases}
\tag{2.2}
$$

These parameters are then used by the software to the positions of the stars into the chosen

reference system. The software that I used, *xym1mat*, developed by Jay Anderson utilizes

this method in order to find the linear transformations parameters between a set of catalogs

in one filter and a reference one of the same filter and, finally, corrects these catalogs trans-

lating them into the reference one. It is to be noted that it is possible to select only stars

present in at least a minimum number (NIMMIN) of catalogs, its value being user-selected.

The program generates output files, one for each catalog given in input, containing posi-

tions and magnitudes in the reference catalog, the transformed values and the residuals of

the transformations; if the program worked correctly residuals should have a close to spher-

ical distribution centered at 0, like in figure 2.6.

Unification of the catalogs in each filter

With the program *xym2bar*, always by Jay Anderson, I created a single catalog for each filter

in which the position magnitude of a star are computed as a mean between each catalog

transformed in the reference frame. At the end of this stage I had one single file for each

filter, with positions and magnitudes for every measured star.

Final Catalogs

The final step is to link together the files obtained with the *xym2bar* program. This was

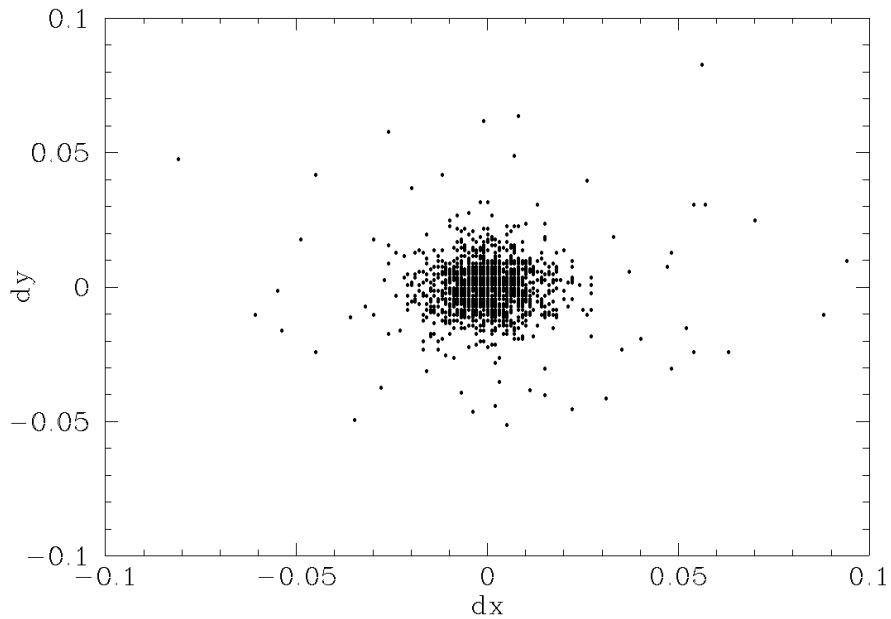done using another software by J. Anderson: *xym1mat*. This program matches two input

Figure 2.6: Plot of the residuals from the transformation between the catalog derived from the image ibcd41cxq and the reference reference one from the image ibcd41cvq, both in the F814W filter.

catalogs in different filters and finds common stars, then writes an output file with their positions and magnitudes. I matched all the filters with the F814W one, I made this choice since this filter had the most stars. To speed up the process, I first linked just bright stars in order to find the transformations, and only then I made the program link all the stars.

2.5 CALIBRATION

The last step in the reduction process is the calibration of the magnitudes using aperture photometry. In order to complete this task I used drz images. This type of images are taken with exposure set at 1 second, so that the pixel values are in fact the numbers of photons per

second. Calibrated magnitudes are the computed as

$$m_{cal} = m_{inst} + \Delta mag + ZP_{filter} + C \qquad (2.3)$$

where Δmag is the difference between the PSF and the aperture photometry magnitude, ZP_{filter}, and C is the aperture correction. The latter two were downloaded from http:// www.stsci.edu/hst/wfc3/analysis/uvis_zpts/uvis1_infinite#r10.

While with aperture photometry, in principle, it is possible to utilize all the flux of the star by simply increasing the aperture radius, it is also true that, if the radius is increased too much even other sources may be included in it. It is really important, then, to determine an ideal radius containing the all the possible flux from the star, in which the aperture is centered, and not any other source. This was done with the program routine *drz_phot_gfortran*, again by J. Anderson. This program computes the aperture photometry given the aperture radius (in pixel) and the inner and outer sky radius. Subsequently I computed the median difference between the PSF and the aperture photometry magnitude, this procedure is shown in figure 2.7. The first step is to select bright not saturated, stars, which are plotted in red in Fig.2.7, because these are better measured. From these stars the first median value is evaluated, with its σ. Then the median is re-evaluated only considering stars in a 2σ interval from the previous value, the procedure is then repeated until the computed value no longer changes.
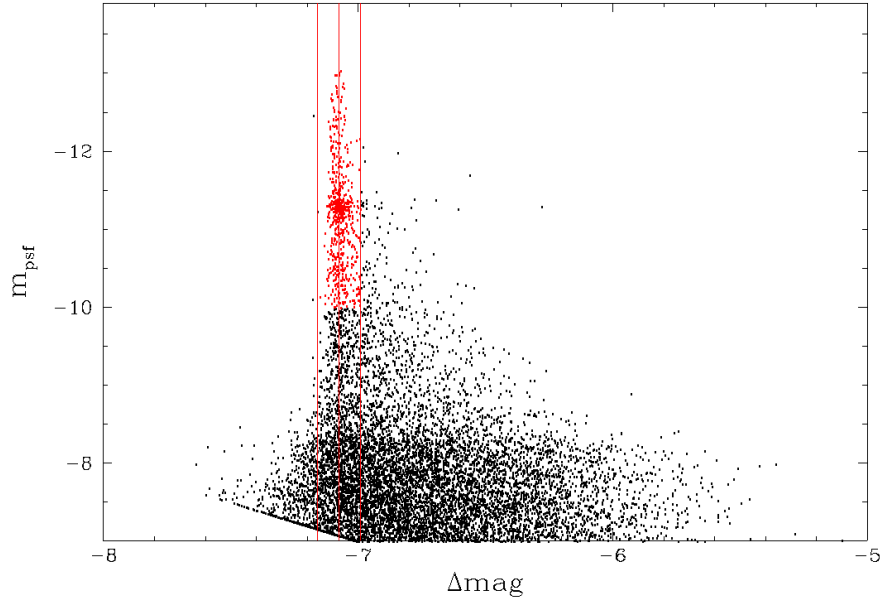
Figure 2.7: Plot showing the procedure to evaluate the median value of the Δmag. In red are the stars selected for the computation; they are included between the two red lines which are at a 2σ from the median value.

2.6 Photometric Errors

I performed artificial-star (AS) experiments to infer the photometric uncertainties and to simulate the photometric diagrams by extending to NGC2419 the procedure by Anderson et al. (2008)[3]. In a nutshell, first a list of coordinates and magnitudes of 100,000 stars was generated. These stars have similar spatial distribution along the field of view as cluster stars and instrumental magnitudes, $-2.5 log_{10}(flux)$, ranging from -13.8 to -4.0 in the F814W band. The other magnitudes are derived from the corresponding fiducial lines of RGB, sub-giant branch, and main-sequence (MS) stars that I derived from the observed CMDs. ASs are reduced by adopting exactly the same procedure used for real stars. The Kitchen Sink 2 computer program derives for ASs the same diagnostics of the photometric and as-

trometric quality calculated for real stars. I included in my investigation only the sample of relatively-isolated ASs that are well fitted by the PSF and have small random mean scatter in magnitudes and positions and that are selected by using the same criteria that I adopted for real stars. With this last operation done the calibration is completed and now it is possible to proceed with the data analysis, in which I will investigate the multipopulations of NGC 2419.

3

Data Analysis

To investigate multiple populations in NGC2419, I exploited the photometric catalogs derived in the previous section to derive the CMDs and the chromosome map of cluster stars. In this chapter I describe the methods that I used to identify the distinct stellar populations along the RGB, to estimate the fraction of stars in each population, and to infer their helium abundance.

## 3.1 Color magnitude diagrams and Chromosome Maps

3.1.1 Color magnitude diagrams

Photometry in appropriate filters is mandatory to identify the distinct stellar populations, furthermore is very important to use filter combinations which are sensible to the abundance variations mentioned previously. For this reason, of particular interest are CMDs built with combinations of the filters F275W, F336W, F343N, F438W and F814W which are sensitive to helium and nitrogen variations. Some of the CMDs obtained with combination of these filters are reported in Fig.3.1

Unfortunately for one of the most used filters in the determination of multiple stellar populations (see Milone et al. 2017 and 2018), F275W, the data used in this work were not ideal. In fact there was only a single image taken in the this filter and of just 400s of exposure time; for this reason the photometry obtained using this filter was too shallow and could not be used to properly identify multiple populations along the RGB of this distant cluster. This can be seen by comparing the various CMDs shown in Fig. 3.1 with the m_{F814W} vs. $m_{F275W} - m_{F814W}$ (the first one) CMD. In this particular CMD the sub giant branch (SGB) stars are too faint to be revealed highlighting the shallowness of the data collected trough this filter.

Two diagrams of crucial interest for the continuation of the data analysis are reported in Figs.3.2 and 3.3. The F438W vs. F438W-F814W CMD of NGC2419 is plotted in Fig. 3.2, where I also show the average observational errors for stars with different luminosities (red error bars). This diagram reveals a tail of stars with bluer colors than the bulk of RGB stars with similar luminosity. This fact provides clear evidence that NGC2419 hosts more than

38
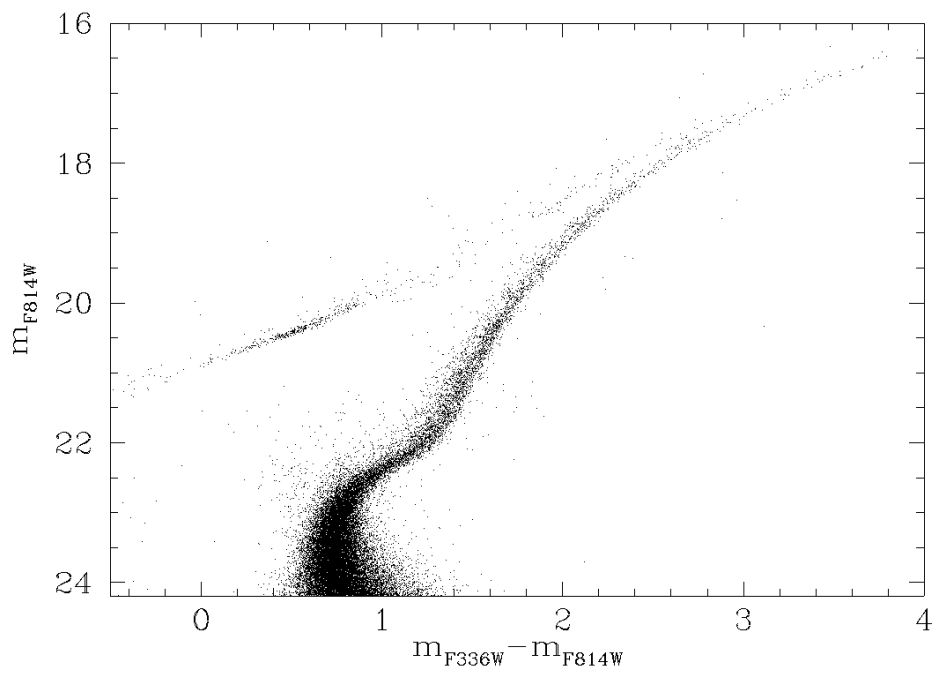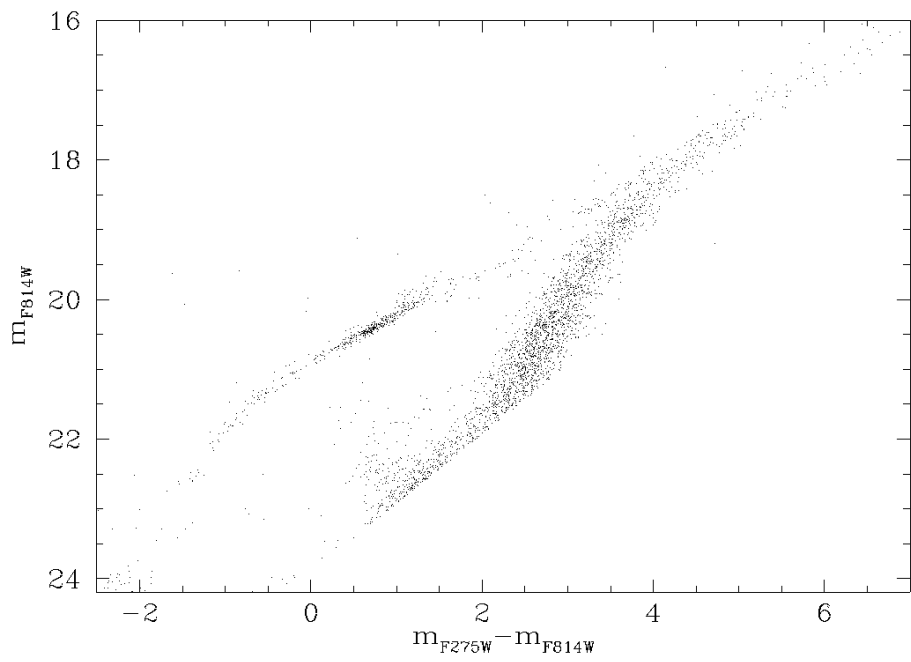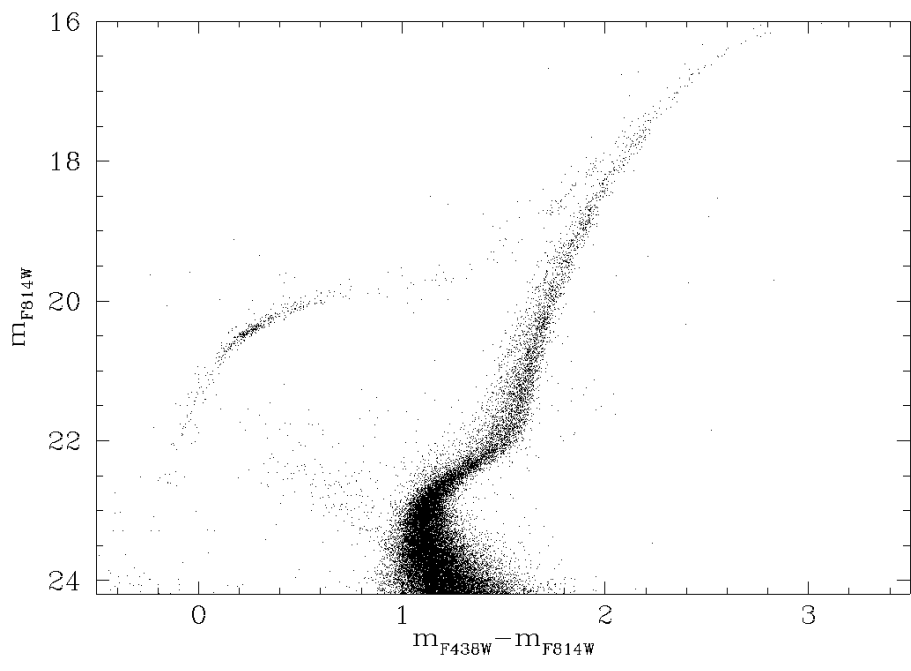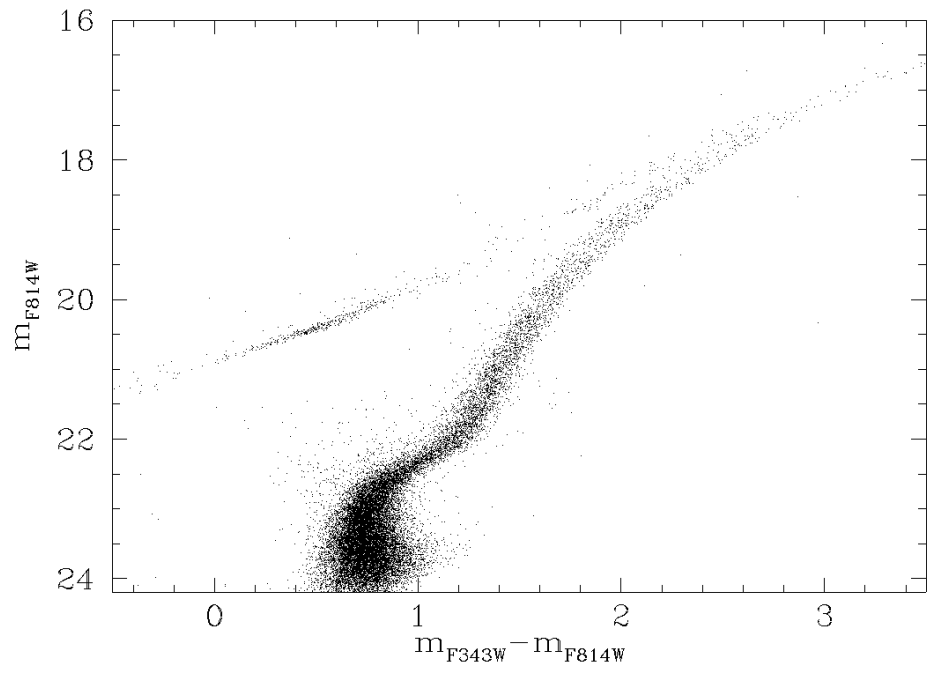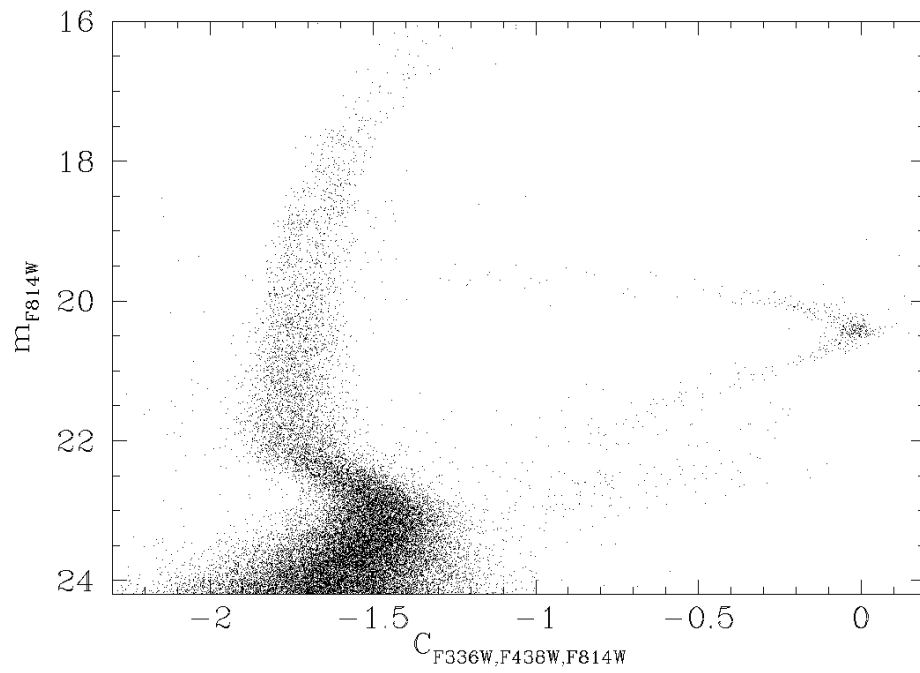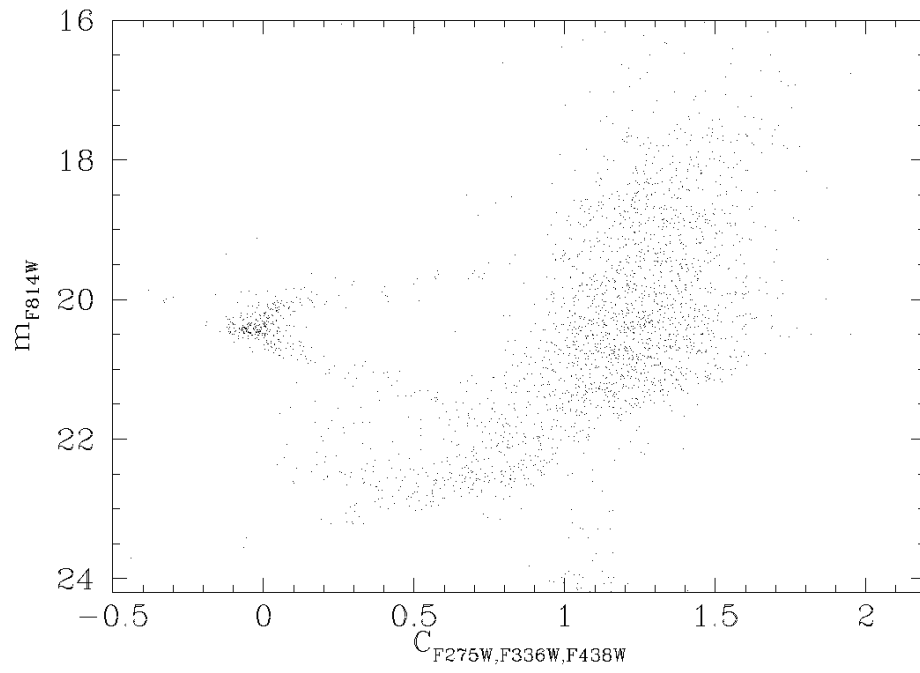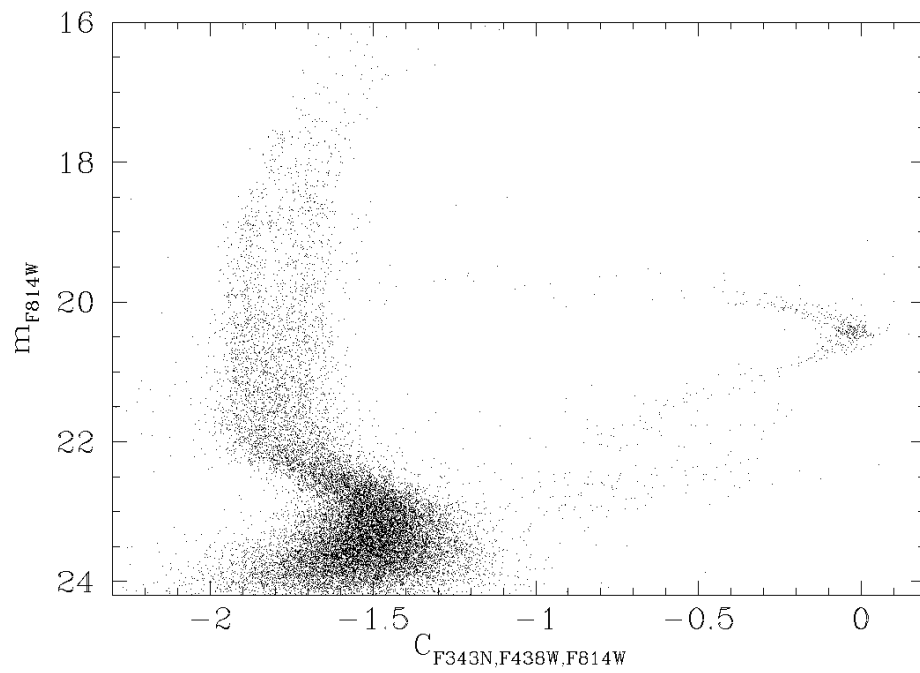
Figure 3.1: Collection of CMDs plotted with the F275W, F336W, F343N, F438W and F814W filters and combinations. These filters are sensible to He and N variations thus are good in identifying different populations.

Figure 3.2: CMD obtained by plotting the star magnitudes in the F438W filter against the magnitude difference of the filters F438W and F814W. The width of the RGB is consistent with the presence of multiple stellar populations. In red are plotted the error bars.

one single stellar population. This translates into a larger RGB than what would be expected from a single population, even considering the photometric uncertainties. The black crosses on both Fig. 3.2 and 3.3 are asymptotic giant branch stars selected 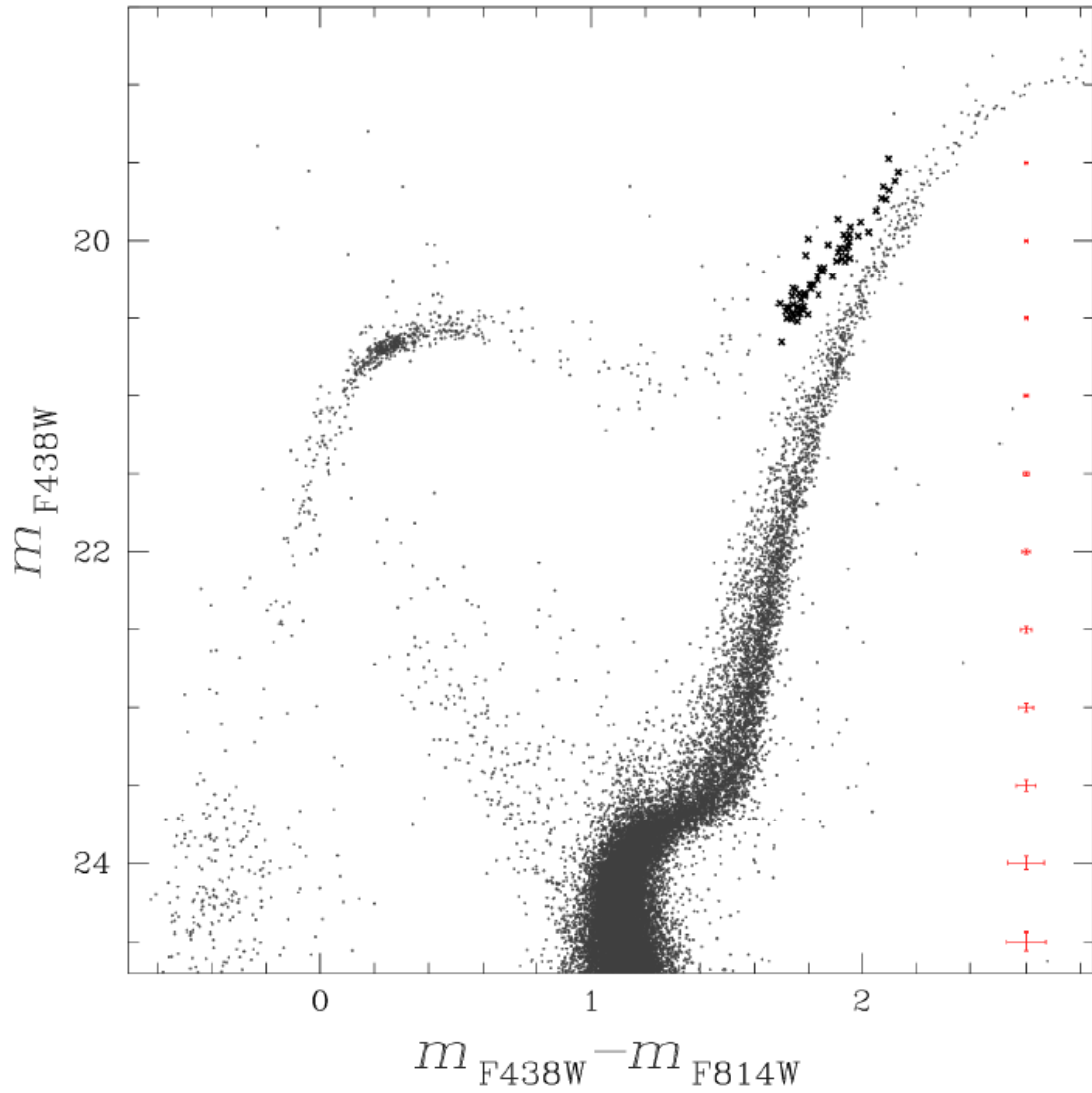from the former figure to compare the broadening in respect to RGB ones as I will explain later. This filter combination, i.e. $m_{F438W} - m_{F814W}$ is an efficient color to identify RGB stars with different effective temperature hence the observed RGB width suggests that NGC 2419 hosts stellar populations with extreme helium abundance.

This hint becomes even more evident if we use a pseudo-colour instead of a colour as explained in chapter 1. For this purpose in Fig. 3.3 is shown the plot the magnitude in the F814W (m_{F814W}) filter against the combination $C_{F336W,F343N,F438W} = (m_{F336W} - m_{F343N}) - (m_{F343N} - m_{F438W})$, again, as in Fig. 3.2, the red bars correspond to the photometric uncertainties and the black crosses are the same AGB stars selected there. This pseudo-CMD, which is particularly sensitive to the abundances of C and N, mostly through the NH and CN bands, reveals a split RGB which is not consistent with a single stellar population cluster. Thus the RGB splits into three different components: a red sequence, a blue sequence, including respectively around 35% and 45% of the total RGB stars, and a third population of stars located between the two main RGBs that comprises about 20% of stars. For the AGB stars it can be noted that although the $C_{F336W,F343N,F438W}$ broadening of AGB stars is larger than the broadening expected from observational errors, these AGB stars span a smaller range of $C_{F336W,F343N,F438W}$ than RGB stars with the same luminosity. This fact indicates that, although the AGB of NGC 2419 is not consistent with a simple population, those 2G stars with extreme chemical composition avoid the AGB phase in close analogy with what is observed in NGC 6752, NGC 6266 and NGC 2808 (Campbell et al. 2013[11];
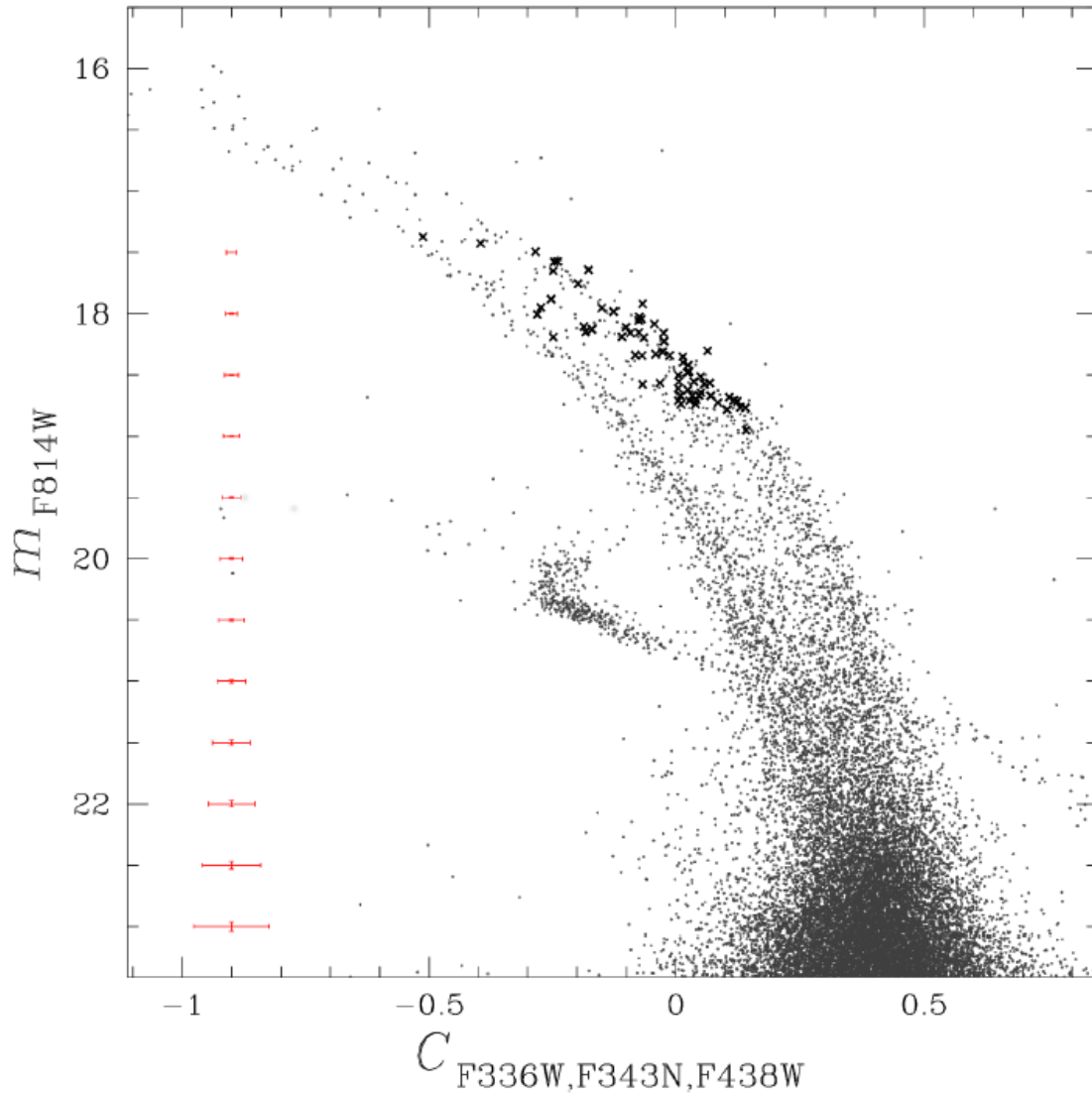
Figure 3.3: m_{F814W} vs. $C_{F336W,F343N,F438W}$ pseudo-CMD. In this plot it is possible to recognize two clearly distinct branches in the RGB and a group of stars between them. The black crosses are AGB stars selected from Fig.3.2; these stars show, indeed, a broadening which is, still, not consistent with a single population. However the width of this broadening is consistently smaller than in the RGB suggesting that 2G stars with extreme chemical composition avoid the AGB phase.

Lapenna et al. 2016[37]; Wang et al. 2016[59]; Marino et al. 2017[39].).

3.1.2 RGB Width

Using the m_{F814W} vs. $m_{f438W} - m_{F814W}$ and the m_{F814W} vs. $C_{F275W,F336W,F438W}$, I was able to measure the width of the RGB two magnitudes above the turn-off (TO) for NGC 2419. Although not ideal, as said previously, I still used the data from the F275W; this decision was taken due to the fact that Milone et al. (2017) calculated the RGB width for 57 globular clusters exploiting the $C_{F275W,F336W,F438W}$ pseudo colour. Thus in order to compare results from this analysis with theirs (see Chapter 4), in spite of being subject to a higher error, I adopted their same choice.

Firstly I selected from the m_{F814W} vs. $m_{f438W} - m_{F814W}$ CMD, reported in Fig.3.1, the MS and RGB stars manually. From this selection I divided the stars in bins of m_{F814W}, calculated the mean $m_{f438W} - m_{F814W}$ value for each bin and finally interpolated between each obtained value; the TO was selected as the 'bluer' point of the fit, i.e. at $m_{F814W} = 23.135$.

This procedure is summarized in Fig.3.4 , where in blue are represented the stars selected as part of the MS and the RGB, in red is portrayed the fitted line and the horizontal red line is placed at the same value of the TO magnitude.

Subsequently, I selected from the m_{F814W} vs. $C_{F275W,F336W,F438W}$ only the RGB stars in a m_{F814W} interval of 0.2 magnitudes centered at $m_{F814W} = 21.138$, two magnitudes above the TO found before. Only stars inside this magnitude interval were considered in the following steps. The values of $C_{F275W,F336W,F438W}$, for the selected sample, were then sorted and the RGB width was computed as the difference between the 96th and 4th percentile. The method described is shown in Fig.3.5 where in red are highlighted the selected sample used
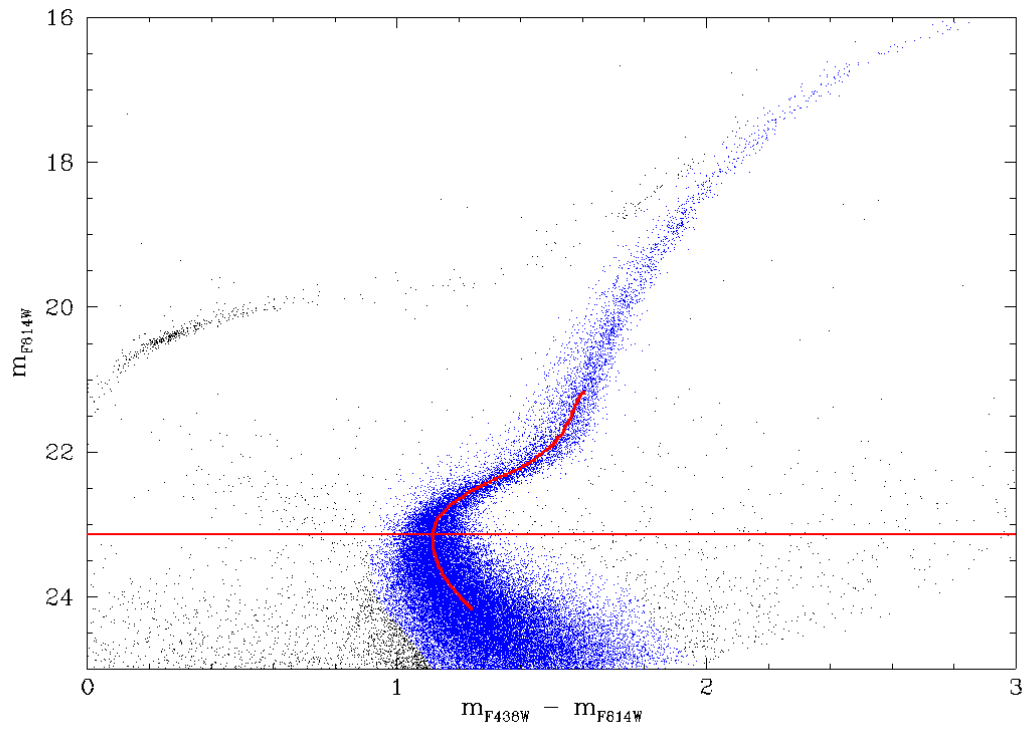
Figure 3.4: In this diagram in blue are represented the stars selected as part of the MS and the RGB, the red line is the result of the fitting process from the mean $m_{f438W} - m_{F814W}$ values in each m_{F814W} bin. Finally the horizontal red line is placed at the same value of the TO magnitude.
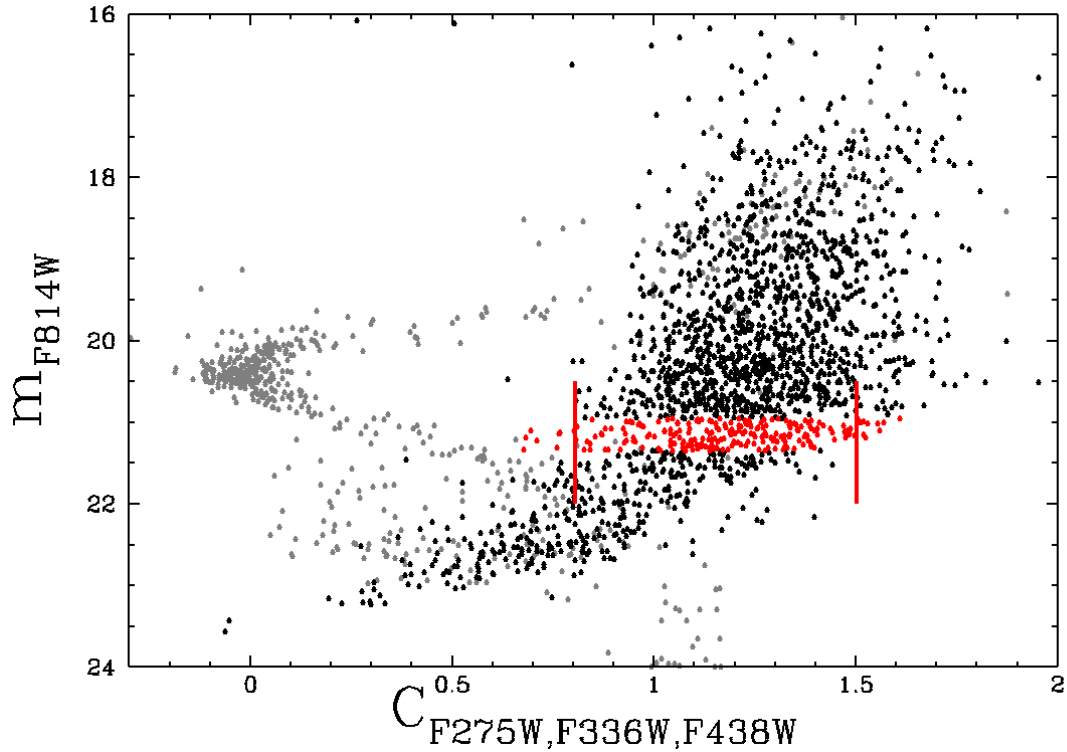
Figure 3.5: Representation of the method used to determine the width of the RGB. In red are plotted the stars selected, for the computation of the width, in a 0.2 magnitude interval around $m_{F814W} = 21.138$. The two vertical lines are placed at the corresponding values for the 96th and 4th percentile of the $C_{F275W,F336W,F438W}$ values for the selection.

for the calculation of the RGB width, the two vertical lines are placed at the corresponding values for the 96th and 4th percentile of the $C_{F336W,F343N,F438W}$ values for the sample.

The value found for the RGB width for NGC 2419 is 0.326.

3.1.3 CHROMOSOME MAP

As anticipated in chapter 1, the chromosome map (ChM) is a powerful tool to recognize and distinguish the multiple stellar population of a globular cluster; as it is derived from the photometry in different filters that are sensitive to the specific chemical composition

of the distinct populations (e.g. Marino et al. 2017[39]; Milone et al. 2017)[44]. The ChM for NGC2419 was built starting from the data displayed in figures 3.2 & 3.3 following the method reported in Milone et al. (2015)[43] and used in by Milone at al. (2017[44], 2018[45]) to derive the chromosome maps for RGB stars in 58 Galactic GCs. They plotted, after the verticalization process (see below), the pseudo colour $C_{F275W,F336N,F438W}$ as a function of the colour $m_{F275W} - m_{F814W}$, with the former mostly sensitive to variations in the nitrogen abundance and the latter sensitive to helium. As explained in the section above the available data in the F275W were far from ideal to be used to retrieve the ChM. As a consequence, a ChM was made by using photometric bands that are different from those used by Milone and collaborators, but are sensitive to helium and nitrogen variations; specifically I used the verticalized $m_{F438W} - m_{F814W}$ colour $\Delta_{F438W,F814W}$ and the verticalized pseudo colour $\Delta_{C_{F336W,F343N,F438W}}$ which is an efficient tool to identify stellar populations with different nitrogen abundance. This verticalization process was done as follows. First of all only RGB stars were manually selected as stars between two fiducial lines, hereafter *bluefiducial* and *redfiducial*, these two fiducial lines mark the 'blue' and 'red' envelope of the RGB. These fiducials are then used to rectify the RGB in such a way that the blue and the red fiducials translate into vertical lines with abscissa equal to −1 and 0, respectively. This is done by defining for each star:

$$\Delta_{F275W,F814W} = \left[\frac{X - X_{bluefiducial}}{X_{redfiducial} - X_{bluefiducial}}\right] - 1 \tag{3.1}$$

$$\Delta_{C_{F336W,F343N,F438W}} = \left[\frac{Y - Y_{bluefiducial}}{Y_{redfiducial} - Y_{bluefiducial}}\right] - 1. \tag{3.2}$$
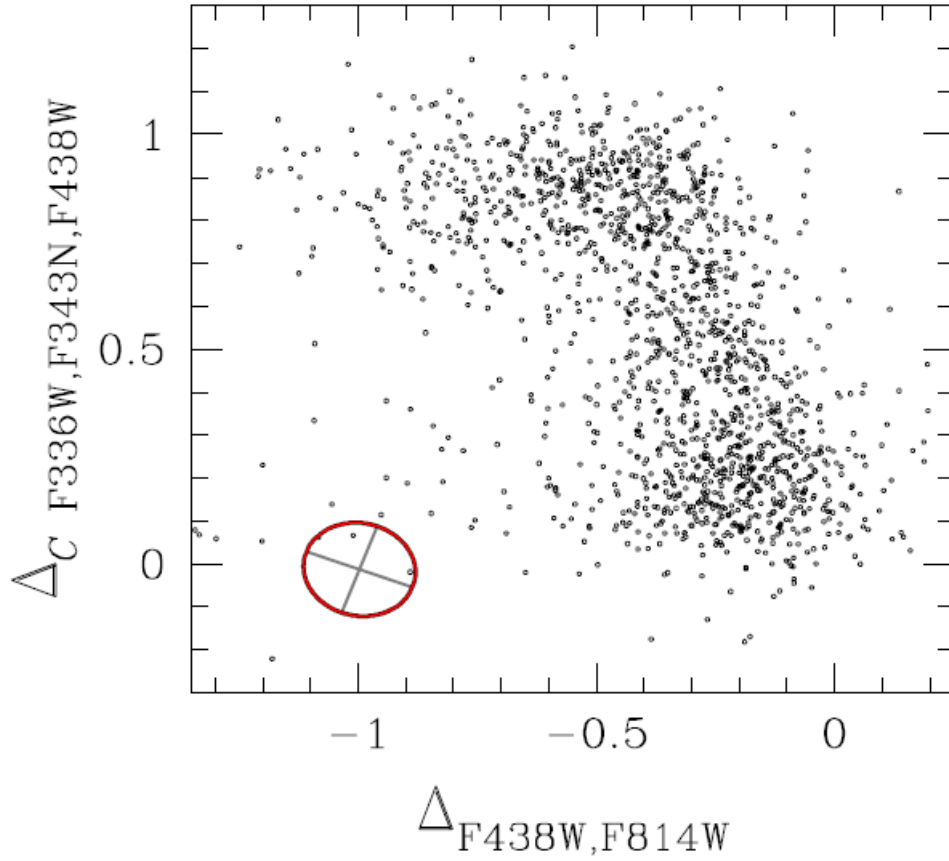
Figure 3.6: Chromosome map obtained from the RGB stars of NGC2419, the red ellipse plotted on the bottom left is indicative of the distribution of the observational uncertainties and is derived from artificial stars

Where $X = m_{F438W} - m_{F814W}$ and $Y = C_{F336W,F343N,F438W}$, while $X_{redfiducial}$, $Y_{redfiducial}$ and $X_{bluefiducial}$, $Y_{bluefiducial}$ are obtained by subtracting the color of the fiducial at the corresponding F814W magnitude from the color of each star. Thus $\Delta_{F275W,F814W} = 0$ and $\Delta_{C_{F336W,F343N,F438W}} = 0$ corresponds to stars lying on the corresponding red fiducial line and the Δ quantities represent the color and pseudo-color distance from such lines.

The result of this procedure is shown in Fig. 3.6 and in Fig. 3.7 where are presented respectively the chromosome map and its Hess diagram. From this images it is possible to

48

Figure 3.7: Hess diagram corresponding to the ChM presented in Fig.3.6. Here the four clumps mentioned there are even more evident.

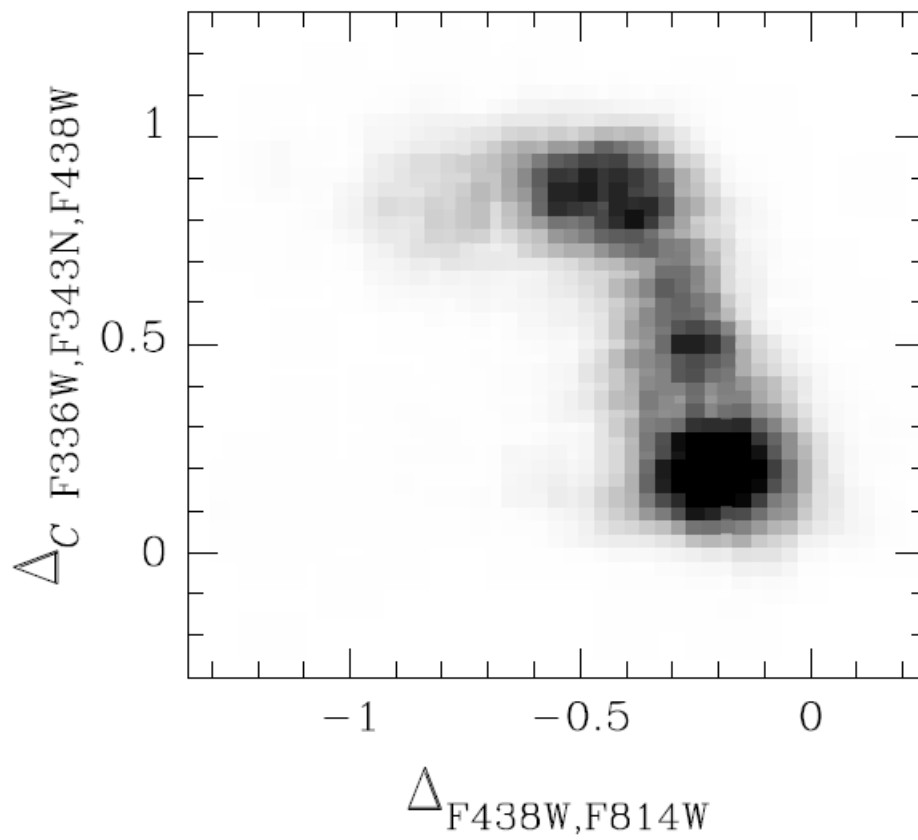recognize four different clusters in the points distribution centered around the coordinates (−0.2,0.2), (−0.3,0.5), (−0.4,0.9) and (−0.8,0.9) respectively. This reveals that NGC 2419 hosts four main stellar populations. In the following section I will show the procedure used to identify these four different populations and determine their relative stellar fractions.

3.2 POPULATIONS OF NGC2419

From the chromosome map (Fig. 3.6) and the corresponding Hess diagram in Fig. 3.7, presented both in the past section, it is possible to begin the proper distinction of the different populations. A procedure similar to the one used by Milone et al. (2017[44], 2108[45]) to define 1G and 2G stars in 58 GCs was adopted.

The starting point is the chromosome map shown in Fig. 3.6. In this diagram 1G stars will be those clustered around the origin of the reference frame, while 2G stars are those in the sequence that reaches large values of $\Delta_{C_{F336W,F343N,F438W}}$. Among the whole 2G stars group it is possible to distinguish 3 sub-populations, named $2G_A$, $2G_B$ and $2G_C$ which are respectively characterized by crescent values of the $\Delta_{C_{F336W,F343N,F438W}}$.

From the ChM I computed the normalized $\Delta_{C_{F336W,F343N,F438W}}$ and $\Delta_{F438W,F814W}$ histogram distributions, see panels (a2) and (a3) of Fig. 3.8. Always in Fig. 3.8 the gray continuous line plotted in panel a2 is the $\Delta_{C_{F336W,F343N,F438W}}$ kernel-density distribution of the observational uncertainties while the black line in panels (a2) and (a3) is the observed distribution in $\Delta_{C_{F336W,F343N,F438W}}$ and $\Delta_{F438W,F814W}$ respectively. This distribution is calculated starting from the gray points (see Fig. 3.8), for these points the adopted value of the $\Delta_{F438W,F814W}$ is chosen arbitrarily while the adopted average $\Delta^{\circ}_{C_{F336W,F343N,F438W}}$ was determined following the method used by Milone et al. (2018) described in the following.

50
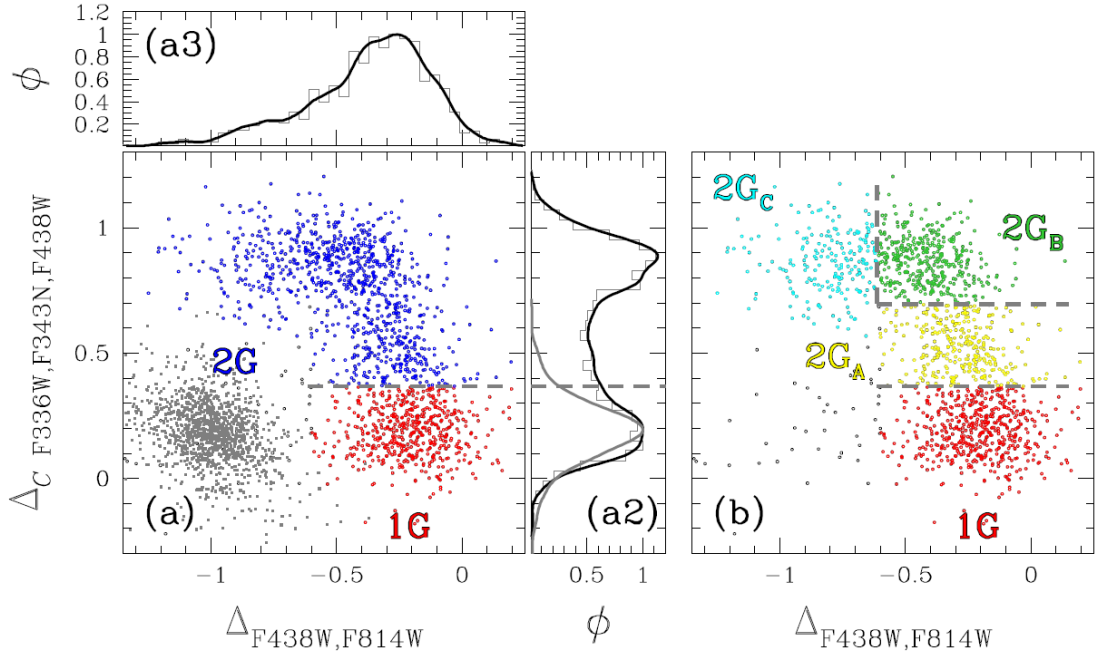
Figure 3.8: This figure illustrates the procedure used to identify the main stellar populations of NGC2419. From the chromosome map the gray points representing the observational errors were added. Panels a2 and a3 show the $\Delta_{C_{F336W,F343N,F438W}}$ and $\Delta_{F438W,F814W}$ histogram distributions, respectively, and the corresponding kernel-density distributions (black lines). The gray continuous line plotted in panel a2 is the $\Delta_{C_{F336W,F343N,F438W}}$ kernel-density distribution of the observational uncertainties, while the horizontal dashed line is used to separate 1G stars from 2G stars, which are colored red and blue in panel a. The four groups of $1G$, $2G_A$, $2G_B$ and $2G_C$ stars are represented with red, yellow, green, and cyan colors, respectively, in panel b.

I assumed various possible values for $\Delta^{\circ}_{C_{F336W,F343N,F438W}}$ and for $\Delta^{i,\circ}_{C_{F336W,F343N,F438W}}$, (i.e. the value in one step) in a range from -0.200 to 0.100 in steps of 0.001. For each step were computed both the $\Delta_{C_{F336W,F343N,F438W}}$ kernel-density distribution of errors, Φ^{i}_{err}, and the observed kernel-density distribution Φ^{i}_{obs}. Hence these two distributions, Φ^{i}_{err} and Φ^{i}_{obs}, were compared, for

$$\Delta_{C_{F336W,F343N,F438W}} < (\Delta^{i,\circ}_{C_{F336W,F343N,F438W}} + \sigma) \tag{3.3}$$

where σ is defined as the 68.27th percentile of the $\Delta_{C_{F336W,F343N,F438W}}$ distribution of the errors, and finally the corresponding χ square was computed. Both distributions are normalized in such a way that their maximum values, calculated in the interval with $\Delta_{C_{F336W,F343N,F438W}} < (\Delta^{i,\circ}_{C_{F336W,F343N,F438W}} + \sigma)$, correspond to one. And finally the adopted value $\Delta^{\circ}_{C_{F336W,F343N,F438W}}$ was selected as the value of $\Delta^{i,\circ}_{C_{F336W,F343N,F438W}}$ that provides the minimum χ square. The dashed gray line plotted in Fig. 3.8 is placed at the $\Delta_{C_{F336W,F343N,F438W}}$ level corresponding to the 1.5σ deviation from $\Delta^{\circ}_{C_{F336W,F343N,F438W}}$ and is used to separate the bulk of 1G stars (red points) from 2G stars (blue points).

The same method was used to differentiate $2G_C$ stars from the rest of 2G stars, except in this case it was exploited the $\Delta_{F438W,F814W}$ distribution. Finally to distinguish $2G_A$ from $2G_B$ stars it was used again the $\Delta_{C_{F336W,F343N,F438W}}$.

The final product of this process is shown in the (b) panel of Fig. 3.8, here, the four different groups 1G, $2G_A$, $2G_B$ and $2G_C$ are portrayed respectively in red, yellow, green and cyan. This final product will be used in the next section to estimate the relative fraction of stars in each population.

3.3   POPULATION RATIOS

At this point it is possible to evaluate the different ratios between the populations of NGC 2419. As anticipated in chapter 1, since this cluster can be considered isolated from the Milky Way influence it is possible that it has retained its initial mass and the fraction of 1G stars (up to $\sim$ 90% of the total). To establish the population ratios in the globular cluster NGC 2419 I used the method adopted by Milone et al. (2012)[46] and adapted to chromosome maps by Nardiello et al. (2018)[49]. This procedure was introduced to estimate the population ratios of different luminosity functions in CMDs and proved to be useful even when applied to ChMs. The reason behind this approach is that due to observational errors some stars could be misplaced in the classification shown in the ChM reported in Fig. 3.8, e.g. a star in the yellow $2G_A$ region could be there not because it shares the same chemical composition as $2G_A$ stars but merely from the uncertainties in its photometrical analysis and this could be the case for every population in each region.

In order to disentangle this problem I calculated for the stars in each population, individuated in section 3.3 and depicted in Fig. 3.8, the average values of $\Delta_{C_{F336W,F343N,F438W}}$ and $\Delta_{F438W,F814W}$ and used these points as centers of four regions, namely R_1, R_{2_A}, R_{2_B} and R_{2_C}. Each region was chosen as an ellipse and similar to the ellipse that reproduces the distribution of photometric uncertainties, the points and the ellipses are shown in panel (a) of Fig.3.9. For the reasons explained above each region could include stars from all the four different established populations. For every region $R_i, i = 1, 2_A, 2_B, 2_C$ it is possible to associate a fraction of stars of each population $f_{R_i}^{1G}, f_{R_i}^{2GA}, f_{R_i}^{2GB}$ and $f_{R_i}^{2GC}$ composing its total
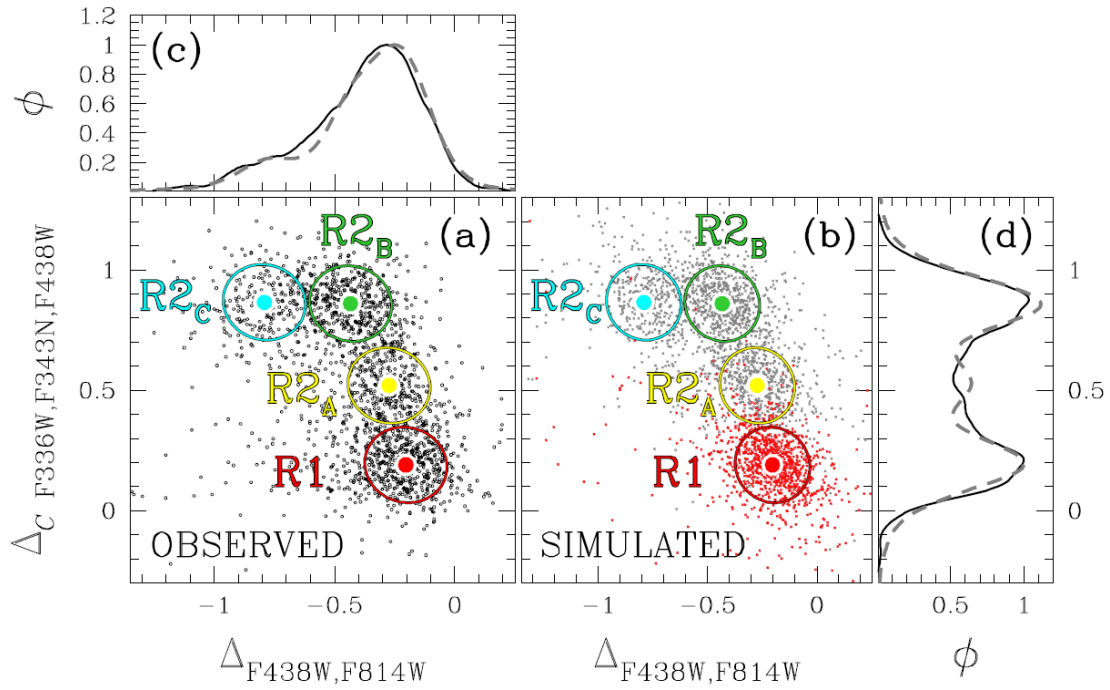
Figure 3.9: Illustration of the method to estimate the population ratios. Panel a is a reproduction of the observed ChM plotted in Fig.3.6 while Panel b shows the simulated ChM. The colored dots are the centers of the four main populations of NGC 2419 while the four regions, R1, R2A, R2B, and R2C used to derive the fraction of stars in each population are represented with red, yellow, green, and cyan ellipses, respectively. The ASs used to simulate 1G stars are colored in red. Panels c and d compare respectively the $\Delta_{F438W,F814W}$ and $\Delta_{C_{F336W,F343N,F438W}}$ kernel-density distributions of observed (black continuous lines) and simulated stars (gray dashed lines).

number of stars:

$$N_{R_i} = N_{1G} f_{R_i}^{1G} + N_{2GA} f_{R_i}^{2GA} + N_{2GB} f_{R_i}^{2GB} + N_{2GC} f_{R_i}^{2GC}, \qquad (3.4)$$

where N_{1G}, N_{2GA}, N_{2GB} and N_{2GC} are respectively the total number of analyzed $1G$, $2G_A$, $2G_B$ and $2G_C$ stars. Before solving the four obtained equations it is necessary to estimate the $f_{R_i}^{1G}$, $f_{R_i}^{2GA}$, $f_{R_i}^{2GB}$ and $f_{R_i}^{2GC}$ values. This was done using artificial stars. With the ASs I reproduced the ChM of NGC 2419 and repeated the same procedures explained above, the result is shown in panel b of Fig. 3.9 in which in red are highlighted the simulated 1G stars. The $f_{R_i}^{1G}$ of 1G stars are then computed as the ratio between the number of ASs within each region and the total number of simulated stars. Finally the system of four equation in eq. 3.4 is solvable and I find that in NGC 2419 the total number of $1G$, $2G_A$, $2G_B$ and $2G_C$ are respectively $37 \pm 1\%$, $20 \pm 1\%$, $31 \pm 1\%$ and $12 \pm 1\%$.

3.4 Chemical Composition of the Stellar Populations

In order to infer the chemical composition of the different population of NGC 2419 the photometry obtained in this work was combined with chemical abundances inferred from spectroscopy in the literature. Mucciarelli et al. in 2012[48] analyzed 49 giants in NGC 2419 using medium resolution spectra collected through the multi-object spectrograph DEIMOS@Keck. They found homogeneous abundances of Fe, Ca and Ti while discovering a large dispersion in the Mg abundance, reaching values of $[Mg/Fe] \sim 1$ (unusual for GC stars), and a very large spread in the K content.

For eleven stars present in the chromosome map of Fig.3.6, Mucciarelli and collaborators
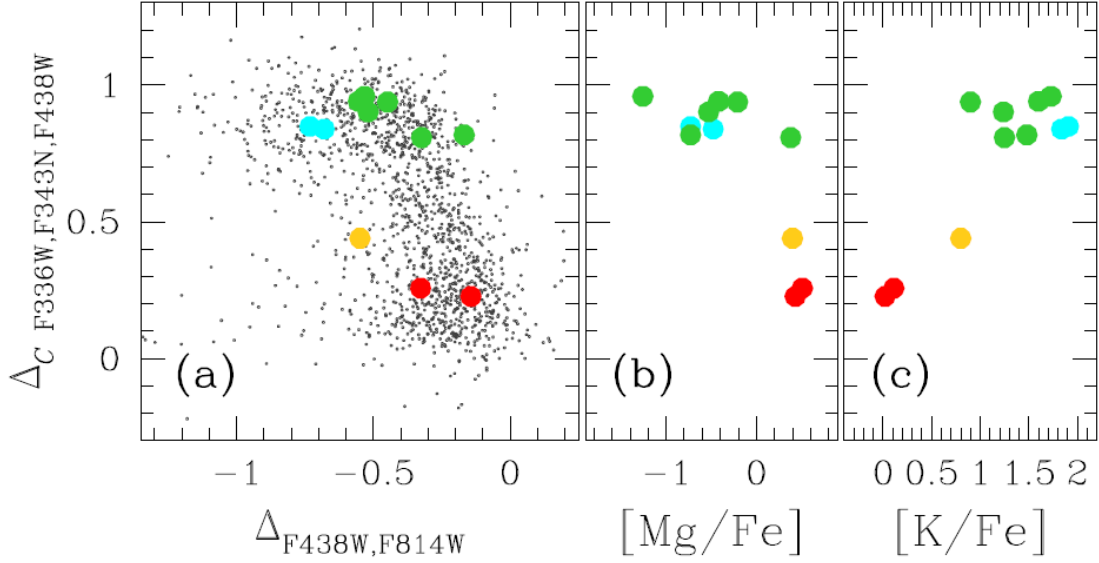
Figure 3.10: Image showing in the ChM the stars for which spectroscopy by Mucciarelli et al. (2012) is available, (large coloured dots). $1G$, $2G_A$, $2G_B$ and $2G_C$ are respectively red, yellow, green and cyan. In panels b and c the same stars are plotted in a $\Delta_{C_{F336W,F343N,F438W}}$ vs [Mg/Fe] and [K/Fe] diagram.

calculated the chemical abundances, of this eleven stars two are $1G$ stars, one is a $2G_A$, six are from the $2G_B$ population and the last two are from $2G_c$. These stars are shown in Fig. 3.10 in which I highlighted them in the ChM (panel a) with the same colours used to distinguish the different populations. In panels b and c of Fig.3.10 the same stars are plotted in a $\Delta_{C_{F336W,F343N,F438W}}$ vs [Mg/Fe] and [K/Fe] diagram; these plots show that $\Delta_{C_{F336W,F343N,F438W}}$ anticorrelates with [Mg/Fe] and correlates with [K/Fe]. In Fig. 3.11 is shown the potassium-magnesium anti-correlation from Mucciarelli et al. (2012).

The comparison between the ChM and the chemical abundances indicates that $1G$ and $2G_A$ stars have similar magnesium abundance of [Mg/Fe]$\sim$0.4, while $2G_B$ and $2G_C$ are depleted in magnesium by ~1 with respect to the remaining stars of NGC2419. $1G$ stars have nearly solar potassium abundance, while the $2G_A$ is enhanced in [K/Fe] by $\sim$0.8. The re-
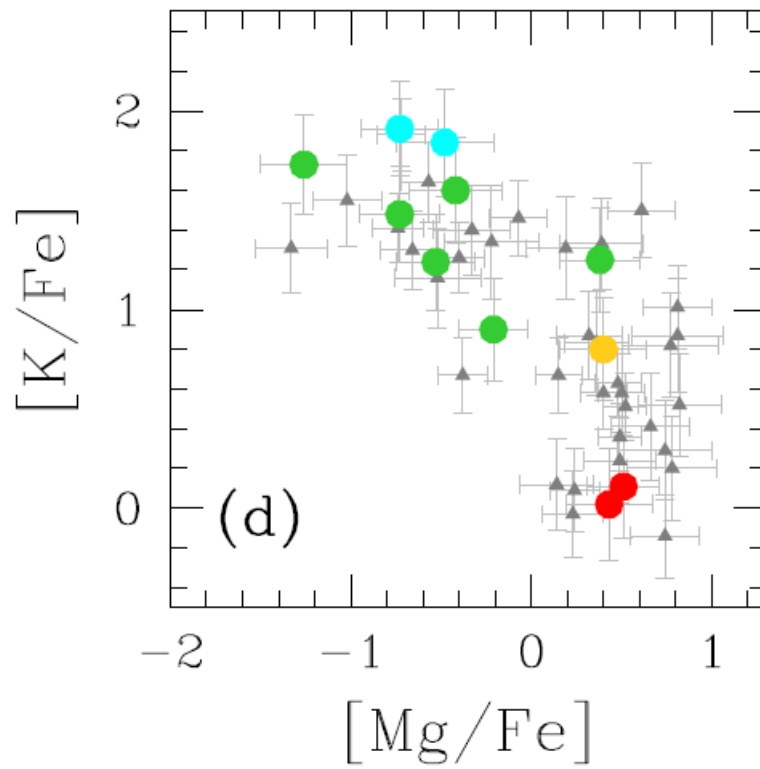
Figure 3.11: Image showing the potassium-magnesium anti-correlation from Mucciarelli et al. (2012). Marked with coloured large dots are the stars present in the ChM of Fig. 3.6.

	1G			2G			$2G_A$			$2G_B$			$2G_C$		
	Average	rms	N	Average	rms	N	Average	rms	N	Average	rms	N	average	rms	N
$[Mg/Fe]$	0.47	0.06	2	-0.40	0.53	9	0.40	0.24	1	-0.46	0.55	6	-0.61	0.18	2
$[K/Fe]$	0.07	0.06	2	1.42	0.40	9	0.80	0.26	1	1.37	0.30	6	1.88	0.05	2
$[Ca/Fe]$	0.31	0.24	2	0.50	0.06	9	0.51	0.07	1	0.49	0.08	6	0.53	0.00	2
$[Fe/H]$	-1.98	0.21	2	-2.08	0.10	9	-2.24	0.13	1	-2.06	0.08	6	-2.06	0.97	2
$[Ti/Fe]$	0.14	0.06	2	0.29	0.10	9	0.34	0.21	1	0.28	0.12	6	0.28	0.01	2

Table 3.1: Average abundance and corresponding random mean scatter (rms) of Mg, K, Ca, Fe, and Ti for 1G, 2G_A, 2G_B and 2G_C stars. I also list the abundances and the corresponding uncertainties of the only 2G_A for which chemical abundances are available. The number, N, of stars used to derive the quoted abundances of each population are also indicated. The elemental abundances are taken from Mucciarelli et al. (2012)[48].

maining stars exhibit extreme potassium contents up to $[\text{K/Fe}] \sim 1.4$ for the six 2G_B stars and $[\text{K/Fe}] \geq 1.9$ for the two 2G_C stars. As discussed by Mucciarelli et al. (2012) there is no evidence for significant variations of Ca, Fe, and Ti. The average elemental abundances for each population are provided in Table 3.1.

3.5 Determination of the Helium abundances

The final result of the data analysis is the determination of the Helium abundances for the different populations of NGC 2419. Before going into the detail of the procedure used for the determination, it is important to remember from chapter 1 that theories, like the supermassive Stars and the AGB ones, on the formation of the multipopulations predict a maximum He content of ~ 0.40.

The main challenge to infer the helium content from spectroscopy is that the helium lines can be detected and used to derive abundances in the spectra of stars that span a small interval of effective temperature, $8000K < Teff < 11500K$, and these conditions are present in only a small number of clusters and stars (e.g.Villanova et al. 2009[58]; Marino et al. 2014)[24].

Therefore in order to determine the relative helium abundances I used the same procedure by Milone et al. (2012, 2018). I started by analyzing the m_{F814W} vs. $m_X - m_{F814W}$ CMDs where X=F225W, F275W, F300X, F336W, F343N, F390W, F438W, F475W, F475X, F555W, F606W, F625W and F775W. From the CMDs I derived the fiducial lines for 1G, $2G_A$, $2G_B$ and $2G_C$ stars, respectively in red, blue, yellow, green and cyan in panels a, b and c of Fig. 3.12 where the procedure is represented for the F275W, F343N and F438W filters. To draw the fiducial lines I firstly divided the RGB into F814W magnitude intervals of size δm, which are defined over a grid of points spaced by magnitude bins of size= $\delta m/3$. For each bin I calculated the median F814W magnitude and X-F814W color, then smoothed these median points by boxcar averaging, where each point has been replaced by the average of the three adjacent points and finally the fiducial lines where drawn by interpolating g the resulting points.

Subsequently I defined four equally-spaced reference points in the magnitude bin $18.0 < m_{F814W} < 20.8$, precisely at the 18.2, 19.0, 19.8, 20.6 magnitude values represented by dashed horizontal lines in Fig. 3.12. At this heights, in magnitudes, I calculated the $m_X - m_{F814W}$ colour difference between the fiducial of the total 2G, the single $2G_A$, $2G_B$ and $2G_C$ and 1G stars for every reference point, this is represented in panels d, e, f and g of Fig. 3.12, in which the coloured dots represent the $\Delta(m_X - m_{F814W})$ values corresponding to the various X filters for the reference point with $m_{F814W}^{ref} = 19.8$.

At this point I derived the gravity and effective temperature of 1G stars, with luminosities that correspond to the reference points, by using the best-fit isochrones from the Dartmouth database (Dotter et al. 2008)[30]. I assumed primordial helium content, $Y = 0.246$, iron abundance, $[Fe/H] = -2.09$ (Mucciarelli et al. 2012)[48], and $[\alpha/Fe] = 0.40$. The best
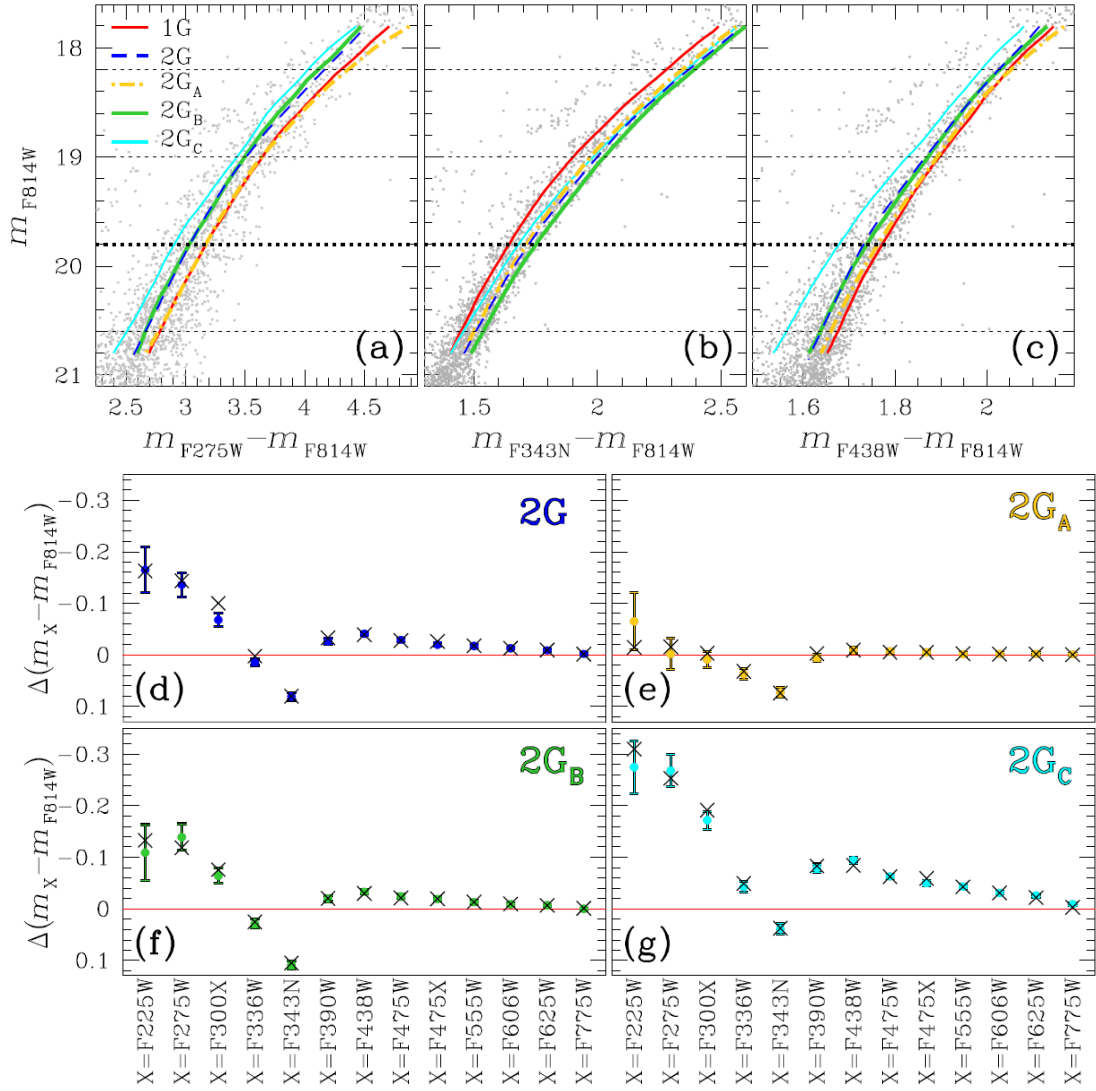
Figure 3.12: In the three upper panels (a), (b) and (c) are shown the different fiducial lines for every population $1G$, $2G$, $2G_A$, $2G_B$ and $2G_C$ respectively in red, blue, yellow, green and cyan in the CMDs built from the $m_{F275W} - m_{F814W}$, $m_{F343N} - m_{F814W}$ and $m_{F438W} - m_{F814W}$ vs. m_{F814W}. The dotted horizontal lines correspond to four magnitude values used to infer the helium abundance of each population. In the four bottom panels (d), (e), (f) and (g) are shown, as coloured dots the observed $m_X - m_{F814W}$ colour difference between the fiducial of $2G$, $2G_A$, $2G_B$ and $2G_C$ with the $1G$ fiducial. All calculated at the $m_{F814W}^{ref} = 19.8$. The colors inferred from the best-fit synthetic spectrum are represented with black crosses.

60

fit between the isochrones and the data, shown in Fig.3.13, is provided by distance modulus and reddening of $(m - M)_0 = 19.68$ and $E(B - V) = 0.07$, respectively, and age of 13.0 Gyr, which are similar to the values listed by Harris (1996, 2010 update)[32] and Dotter et al. (2010)[31].

For each reference point I calculated a synthetic spectrum and a grid of comparison spectra with different chemical composition by using the computer programs ATLAS 12 and Synthe (Kurucz 2005[36]; Castelli et al. 2005[14]; Sbordone et al. 2007[54]). I assumed [C/Fe]= −0.6, [N/Fe] = 0.6, [O/Fe] = 0.4, as inferred from high-resolution spectra of 1G stars in the metal-poor GC M22 by Marino et al. (2011)[40], and the values of effective temperature and gravity that I derived from the best-fit isochrone and are provided in Tab. 3.2. The comparison spectra have [C/Fe] that ranges between −1.5 and 0.0 and [O/Fe] that ranges from −1.0 to 0.4 in steps of 0.1. [N/Fe] varies from 0.30 to 2.00 in steps of 0.05. The helium content of the comparison spectra ranges from Y=0.246 to 0.470 in steps of 0.001 and the values of effective temperature and gravity are derived from the corresponding isochrone from Dotter et al. (2008)[30]. The magnesium content is fixed and corresponds to the average [Mg/Fe] abundances of 1G and 2G stars inferred from the data by Mucciarelli et al. (2012)[48] and listed in Table 3.1.

The corresponding color differences have been derived from the convolution of each spectrum with the transmission curves of the WFC3/UVIS filters used in this thesis. The best determinations of the relative helium content between 2G and 1G stars are given by the chemical composition of the comparison spectrum that provides the best match with the observed color differences and correspond to an helium difference $\delta Y_{2G-1G} = 0.07 \pm 0.01$, where the uncertainty is estimated as the rms of the four helium determinations divided
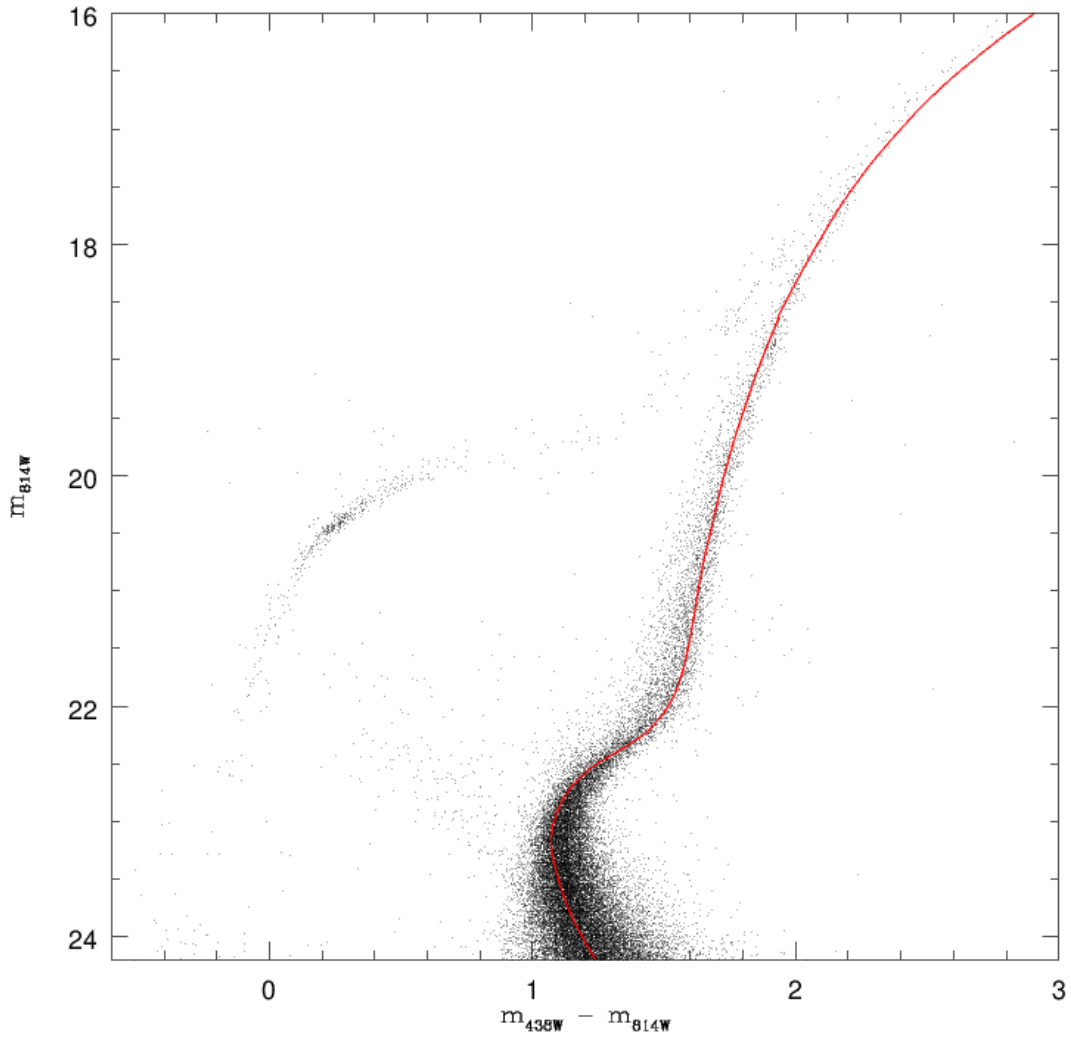
Figure 3.13: Image showing the best-fit iscohrone, from the Darthmouth database (Dotter et al. 2008), in red , over the m_{F814W} vs. $m_{F438W} - m_{F814W}$. The fit was obtained assuming the distance modulus and the reddening of $(mM)_{\circ} = 19.68$ and $E(B - V) = 0.07$, respectively, and with an age of 13.0 Gyr.

by the square root of three. As an example, the black crosses plotted in panel d of Fig. 3.12 represent the color differences corresponding to the spectra that provide the best fit with the observed color difference between 2G and 1G stars for $m^{ref}_{F814W} = 19.8$.

The procedure described above has been also used to infer the relative abundances of He between $2G_A$, $2G_B$, $2G_c$ and 1G stars. Results are listed in Table 3.2 for each value of m^{ref}_{F814W}, while in panels f, g, and e of Fig. 3.12 I show the observed difference between the color of each population and the color of 1G stars for $m^{ref}_{F814W} = 19.8$ and the corresponding color differences inferred from the best-fit spectra.

I conclude that 2GA, 2GB, 2GC are enhanced in helium mass fraction by 0.01 ± 0.01, 0.06 ± 0.01, and 0.19 ± 0.02, respectively, with respect to 1G stars. The procedure that I adopted to infer the helium content of the stellar populations also allows to constrain the relative abundances of C, N, and O (see Milone et al. 2015, 2017 for details). From the best-fit spectra I find that $2G_A$ are enhanced in nitrogen by 0.3 ± 0.1 and depleted in C and O by 0.3 ± 0.3 and 0.2 ± 0.2, respectively, with respect to 1G stars. $2G_B$ stars exhibit higher [N/Fe] than the 1G (by 0.7 ± 0.1), and lower [C/Fe] and [O/Fe] (by 0.6 ± 0.2 and 0.5 ± 0.1, respectively). The $2G_C$ is enhanced in nitrogen by 0.7 ± 0.1 and depleted in carbon and oxygen by 0.7 ± 0.3 and 0.6 ± 0.2, respectively, with respect to 1G stars.

m_{F814W}^{ref}	1G		2G			$2G_A$			$2G_B$			$2G_C$		
	T_{eff}	log g	T_{eff}	log g	δY	T_{eff}	log g	δY	T_{eff}	log g	δY	T_{eff}	log g	δY
18.2	4844	1.73	4881	1.69	0.070	4842	1.73	−0.003	4871	1.70	0.052	4926	1.62	0.173
19.0	5006	2.10	5038	2.07	0.055	5006	2.10	0.000	5033	2.07	0.047	5086	2.00	0.153
19.8	5157	2.47	5206	2.42	0.078	5162	2.47	0.008	5139	2.44	0.058	5274	2.33	0.208
20.6	5286	2.82	5340	2.79	0.073	5298	2.81	0.017	5331	2.79	0.061	5436	2.68	0.219

				Average							
2G			$2G_A$			$2G_B$			$2G_C$		
δY	rms		δY	rms		δY	rms		δY	rms	
0.069	0.010		0.006	0.009		0.055	0.006		0.188	0.031	

Table 3.2: Atmospheric parameters and helium variations of the best-fit spectra inferred for the four reference magnitudes and average helium variations.

4

Discussion and Conclusion

With the completed data analysis presented in Chapter 3 it is possible to look at the obtained results and to compare them with both the model predictions mentioned in Chapter 1 and with other studies in the same context.

In the first section of this chapter I summarize the data reduction and analysis processes and present the obtained results. In the second I compare the work made in this thesis with

the model predictions and with other works in the literature.

4.1 Results

In this work I reduced HST images in 14 different filters, of the UVIS/WFC3 camera, using the programs by J. Anderson. These programs through the use of the effective-PSF allowed me to retrieve extremely accurate photmetric measurements of the stars of the massive outer-halo globular cluster NGC 2419.

These measurements were, then, used to investigate the multipopulations in the GC. This was done trough the use of the chromosome map: I built the ChM starting from the the RGB stars of the $m_{F438W} - m_{F814W}$ vs. m_{F438W} and the $C_{F336W,F343N,F438W}$ vs. m_{F814W} CMDs shown in Fig. 3.2 and 3.3; I verticalized these CMDs following the procedure from Milone et al. (2015) obtaining the verticalized colour $\Delta_{F438W,F814W}$ and the verticalized pseudo-colour $\Delta_{C_{F336W,F343N,F438W}}$; finally the ChM in Fig. 3.6 is the plot of this two quantities. From the analysis of the ChM and following the methods and procedures explained in the sections 3.3 and 3.4 I identified four different populations in NGC 2419 which I called $1G$, $2G_A$, $2G_B$ and $2G_C$, as seen in Fig. 3.8. These four groups of stars host respectively $37 \pm 1\%$, $20 \pm 1\%$, $31 \pm 1\%$ and $12 \pm 1\%$ of the total stars of the cluster.

Spectroscopic investigation has revealed that NGC 2419 exhibits extreme star-star-abundance variation in Mg and K (Cohen et al. 2011, 2012) with an extended Mg-K anti-correlation (Mucciarelli et al. 2012) Fig, 3.11. Mucciarelli and his collaborators analyzed 49 giants in NGC 2419 using medium resolution spectra collected through the multi-object spectrograph DEIMOS@Keck. Eleven of their stars are RGB stars present in the ChM of Fig. 3.10: two are 1G stars, one is a $2G_A$, six are from the $2G_B$ population and the last two are from

$2G_c$. From these stars I inferred that $1G$ and $2G_A$ stars have similar magnesium abundance [Mg/Fe]~0.4, $2G_B$ and $2G_C$ are depleted in magnesium by ~1 with respect to the remaining stars of NGC2419. $1G$ stars have nearly solar potassium abundance, while the $2G_A$ are enriched in [K/Fe] by ~ 0.8; the remaining stars exhibit extreme potassium contents up to [K/Fe] ~ 1.4 for the $2G_B$ ones and $[K/Fe] \geq 1.9$ for the stars belonging to the $2G_C$ population.

The final result of this work was the determination of the He abundances of the different MPs of NGC 2419; in order to retrieve them I followed the method by Milone et al. (2012,2018) and explained in sect. 3.6: I computed the fiducial lines in the CMDs of each filter (m_{F814W} vs. $m_X - m_{F814W}$) for every population, then at four m_{F814W} values I calculated the difference between the fiducial lines with respect of the $1G$ fiducial lines. Then I derived the gravity and effective temperature of $1G$ stars with luminosities that correspond to the four reference points by using the best-fit isochrones from the Darthmouth database (Dotter et al. 2008). Using the programs ATLAS 12 and Synthe for each of the four points I calculated a synthetic spectrum and a grid of comparison spectra with different chemical composition. The chemical composition of the comparison spectrum that provides the best match with the observed colour differences of the fiducials is chosen as the correct one. Assuming a primordial helium content for the $1G$ population Y=0.246 I find that the total 2G-1G helium difference at $\delta Y_{2G-1G} = 0.07 \pm 0.01$ while the different $2G_A$, $2G_B$ and $2G_C$ are enhanced respectively by 0.01 ± 0.01, 0.06 ± 0.01, and 0.19 ± 0.02.

4.2 Discussion

4.2.1 Population Ratios

I anticipated in chapter 1 that NGC 2419 is one the most interesting globular clusters to test the current theories on the origin of the multiple stellar populations. Some of this theories, suggest that the globular clusters we observe nowadays are 'small' remnants of much more massive objects, that lost most of their '1G' or 'first population' stars due to tidal stripping from their host galaxy. In particular, since 2G stars formed in the innermost cluster regions, the primordial GCs preferentially lost 1G stars (e.g.D'Ercole et al. 2008[27], 2010[26]; D'Antona et al. 2016[20]). Thus observing far away GC could provide interesting results. As said before, NGC 2419 is distant $\sim 87.5 kpc$ from the galactic center; this makes it almost isolated from the tidal influence of the Milky Way and, therefore, a perfect candidate to have retained almost all its 1G stars. 1G stars in this cluster would be expected to represent up to 90% of total stellar component of NGC 2419.

However from the analysis made in this work the 1G stars of this faraway cluster are only the $37 \pm 1\%$ of the total, which is much less than what expected. To better understand the situation it is useful to look at Fig. 4.1, here I plotted the fraction of 1G stars with respect of the total RGB stars against the cluster distance from the MW. In this plot NGC2419 is represented as a blue triangle, and the 58 GCs analyzed in Milone et al. (2017, 2018) as black circles. In this image we can see that, despite the large gap in distance between NGC 2419 and the other clusters, it does not show an increased fraction of 1G stars.

In Figs. 4.2 and 4.3 I show the plots of the fraction of 1G stars against respectively the cluster absolute visual magnitude and mass (both taken from Harris 1996, updated as in
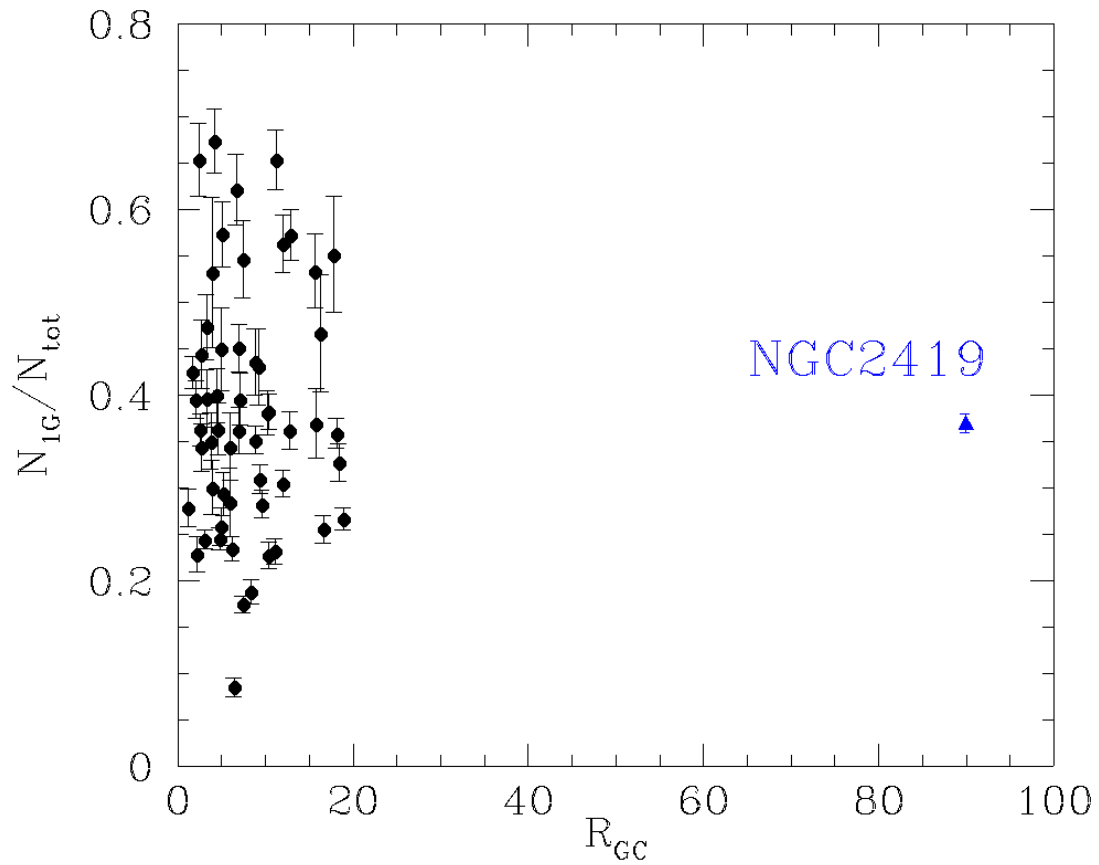
Figure 4.1: Fraction of 1G stars versus the distance from the center of the Milky Way of the 58 GCs analyzed in Milone et al. (2017, 2018), as black circles, and of NGC 2419, the blue triangle.It appears evident that the cluster studied in this thesis is extremely far away from the MW with respect of those already examined by Milone and collaborators. However NGC 2419 does not show a particularly high fraction of 1G stars as some theories would predict from an almost isolated cluster.
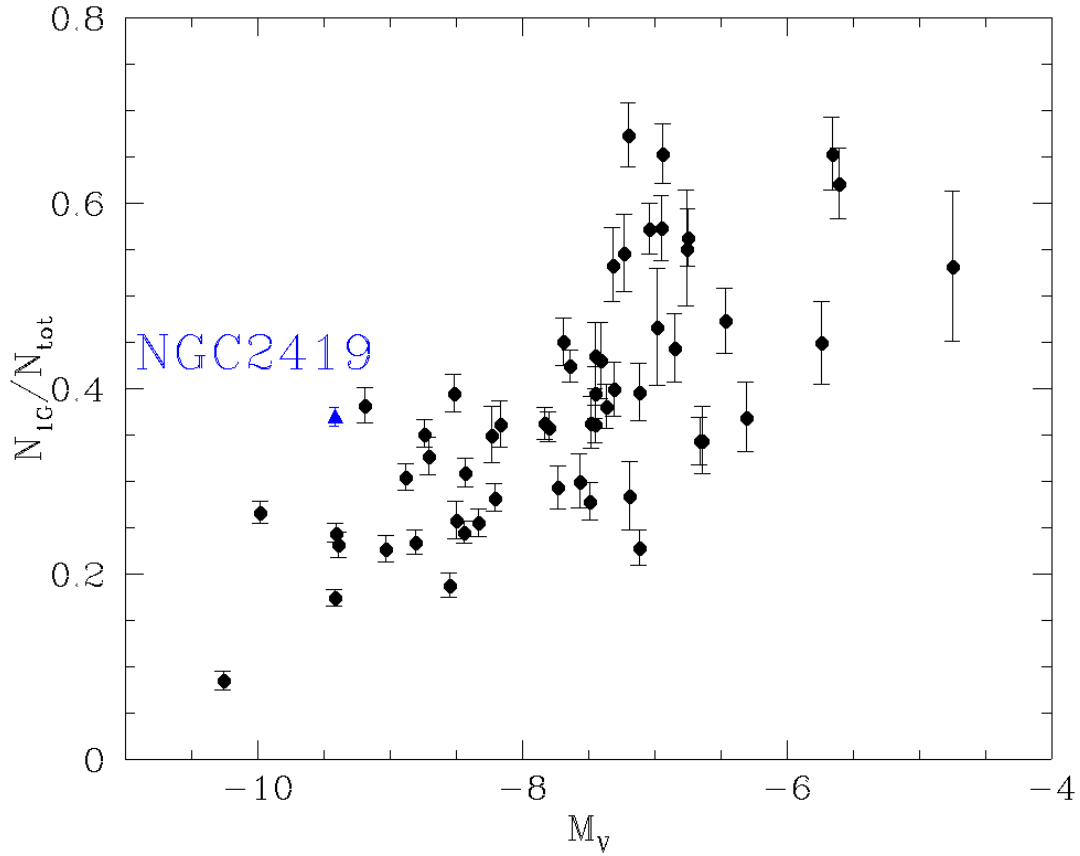
Figure 4.2: Fraction of 1G stars versus the absolute magnitude (from Harris 1996, updated as in 2010) of the 58 GCs analyzed in Milone et al. (2017, 2018), as black circles, and of NGC 2419, the blue triangle.

2010) of NGC 2419, the blue triangle, and the 58 clusters from Milone et al. (2017, 2018). While it is true that NGC 2419 hosts a larger fraction of 1G stars than the clusters of the same absolute magnitude and mass, thus going in favour of theories predicting a larger fraction of such stars in more distant clusters, the measured 37% is still considerably lower than expected.

The information presented to this point can be combined to obtain Fig. 4.4. In the right panel of this image are plotted the fraction of 1G star against the perigalactic distance R_{PER}
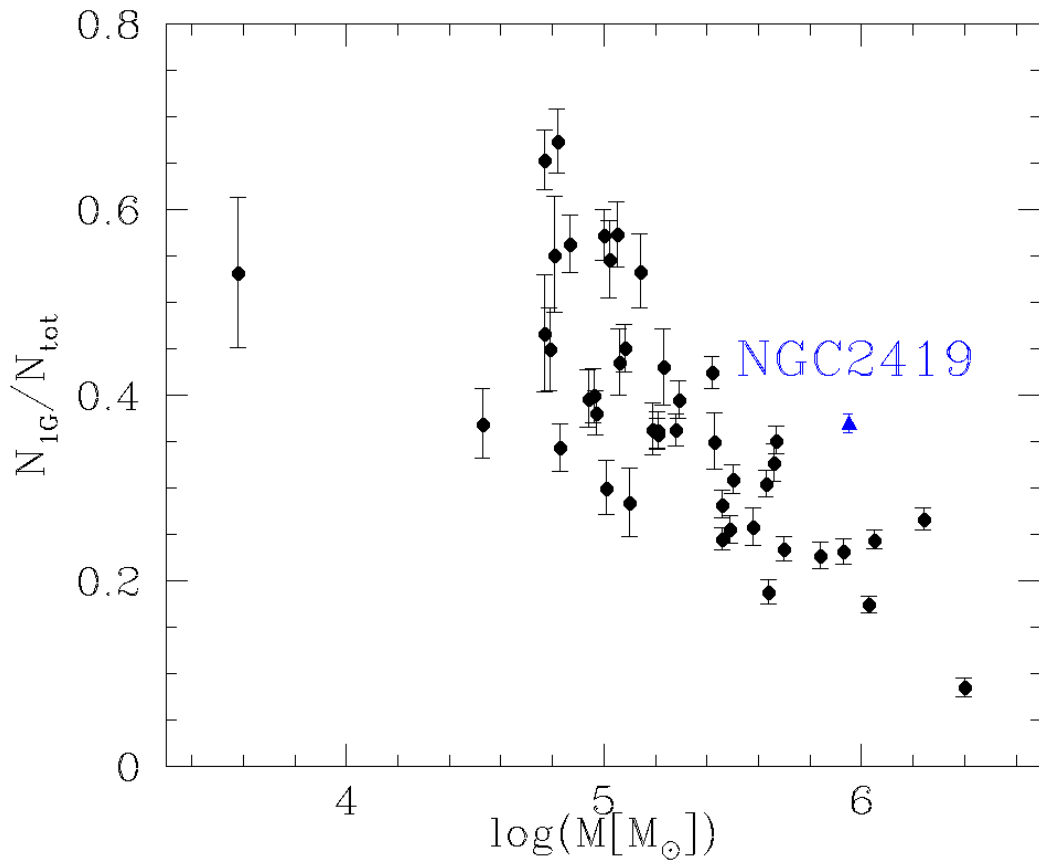
Figure 4.3: Fraction of 1G stars versus the mass (from Harris 1996, updated as in 2010) of the 58 GCs analyzed in Milone et al. (2017, 2018), as black circles, and of NGC 2419, the blue triangle.
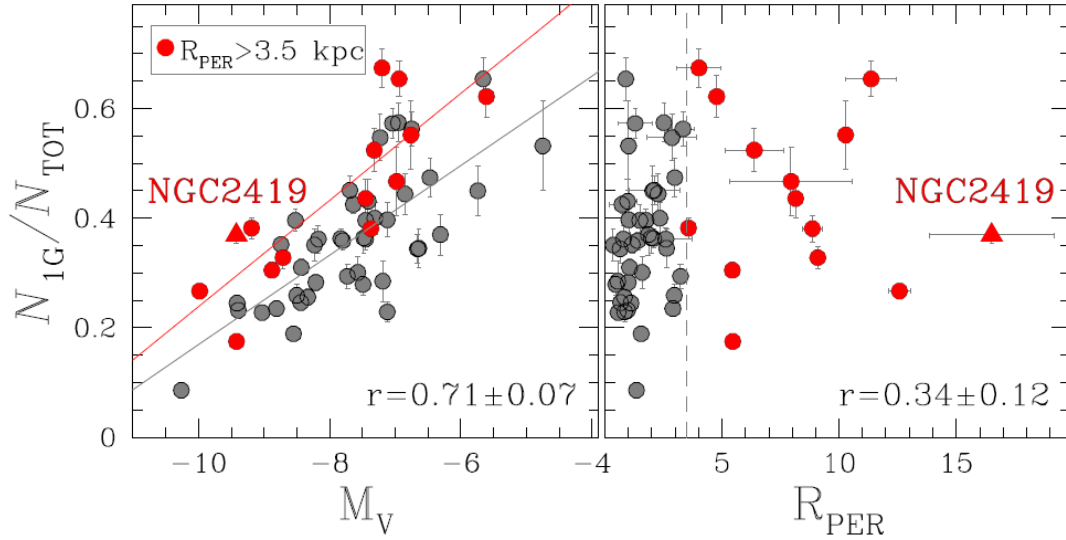
Figure 4.4: Right panel: absolute visual magnitude (from Harris 1996, updated as in 2010) against the fraction of 1G stars for NGC 2419, as a triangle, and the 58 GCs from Milone et al. (2017, 2018) as circles. Left panel: plot of the perigalactic distances (from Baumgardt et al. 2019) against the fraction of 1G stars of the same clusters. In both panels clusters with $R_{PER} > 3.5$ are plotted in red, the others are in gray. In the left panel the two lines represent the corresponding least-squares best-fit of the stars with $R_{PER} > 3.5$ in red and the others in gray.

of the host GC (obtained from Baumgardt et al. 2019[6], $r = 0.34 \pm 0.12$) of the same GCs as before; the triangle is NGC 2419, and in red clusters with perigalactic distance larger than 3.5 Kpc are highlighted. In the left panel the 1G fraction is plotted against the absolute visual magnitude as for Fig. 4.2 but with the same clusters in red as in the right panel. In the left panel of Fig.4.4 the two lines represent the corresponding least-squares best-fit of the stars with $R_{PER} > 3.5$ (in red) and all the others (in gray). it is noteworthy that further clusters from the MW show, on average higher 1G fractions.

To draw conclusions in NGC 2419 the fraction of 1G stars is indeed larger than in other clusters with similar masses and luminosities, thus suggesting that the interaction between the cluster and the Galaxy can affect its present-day ratio between 2G and 1G stars. On the

other hand the presence of 2G population including more than 60% of the total number of cluster stars of NGC2419 is a challenge from the scenarios that predict for this isolated cluster a fraction of 1G of $\sim$ 90% of the total.

4.2.2 HELIUM ABUNDANCES

The second important result of this work is the determination of the He abundance variations between the four different population of NGC 2419: $2G_A$, $2G_B$ and $2G_C$ are enhanced respectively by 0.01 ± 0.01, 0.06 ± 0.01, and 0.19 ± 0.02 with an assumed primordial composition of 1G stars (Y=0.246) the maximum He abundance for $2G_C$ stars would be $Y_{max} = 0.436$.

As anticipated in Chapter 1 many theories on the formation of multiple populations in globular clusters proposed that 2G stars formed by the ejecta of more massive 1G stars. The nature of the polluters is still widely debated. AGB stars with masses of $\sim$ 3 $-$ 8$M_\odot$ (e.g. Ventura et al. 2001[57]; D'Antona et al. 2002[18], 2016[20]; Tailo et al. 2015[56]), fast-rotating massive stars (FRMSs, Decressin et al. 2007[22]; Krause et al. 2013[35]), and super-massive stars (Denissenkov et al. 2014[24]) are considered as possible candidates.

Populations with extreme helium content are a challenge for both the AGB and the super-massive stars models which predicts a maximum He content in 2G star of $\simeq$ 0.38 (although Karakas et al. (2014)[34] suggested that such stars with extreme helium content can form from the ejecta of a previous generation of helium-rich AGB stars) and $Y \sim$ 0.40. On the other hand, the presence of stars with extreme helium abundance is consistent with the FRMSs scenario, e.g. Chantereau et al. (2016)[15], based on this model, predicted that about 10% of present-day GC stars have $Y > 0.40$, which is qualitatively consistent with what we

observe in NGC 2419, however the lack of stars with very high helium content ($Y > 0.50$) is in contrast with the predictions by Chantereau and collaborators.

It is worth to add the results found, in this work, for NGC 2419 to the ones previously obtained by Milone and his collaborators on the same other 58 GCs mentioned in the previous section. In their work they found that the maximum internal helium variation correlates with the mass of the host GC with more massive clusters hosting populations with larger He differences and correlates with the absolute visual magnitude, i.e. more luminous clusters show higher maximum He variations.

This can be seen in Fig. 4.6 and 4.5 in which are shown the plots of the maximum helium variation in the GCs against the logarithm of the mass and absolute visual magnitude respectively for both the 58 GCs mentioned in the previous section (black) and NGC 2419 (blue). NGC 2419 being among the most massive globular clusters in the MW shows, by far, the highest measured helium variation between its populations suggesting that the complexity of multiple populations increases with cluster mass.

4.2.3   RGB WIDTH

Finally in this last section compare the RGB width found in this work with the results presented in Milone et al. (2016). In their work they tried to relate multiple populations properties to the global parameters of the host GCs. Such global GC parameters includes: metallicity ([Fe/H]), absolute visual magnitude (M_V), central velocity dispersion (σ_v), ellipticity (ε), central concentration (c), core relaxation time (τ_c), half-mass relaxation time (τ_{hm}), central stellar density (ϱ_o), central surface brightness (μ_V), reddening (E(B − V)), and Galactocentric distance (R_{GC}). One of these trials they made was with the RGB width.
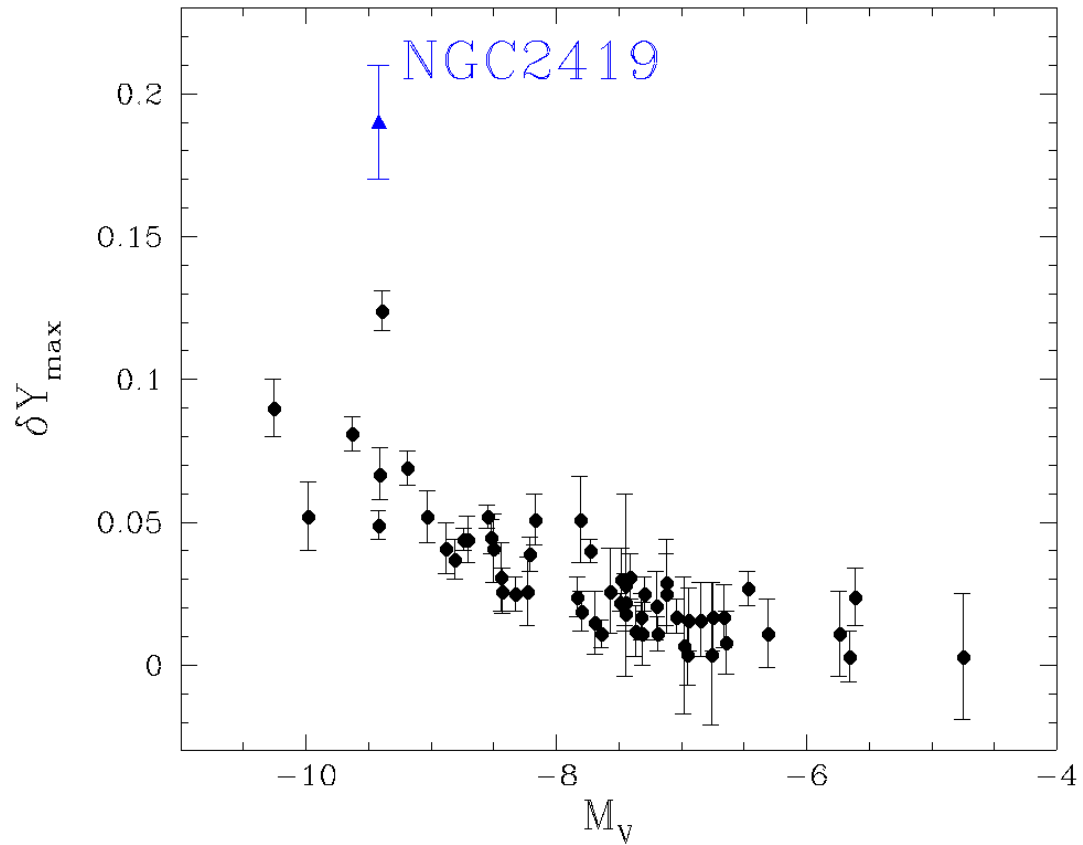
Figure 4.5: Image showing the plot between the maximum He variation between the cluster populations and the GCs absolute visual magnitudes (from Harris 1996, updated as in 2010) of the 58 GCs analyzed in Milone et al. (2017, 2018), as black circles, and of NGC 2419, the blue triangle.

Figure 4.6: Image showing the plot between the maximum He variation between the cluster populations and the GCs masses (from Harris 1996, updated as in 2010) of the 58 GCs analyzed in Milone et al. (2017, 2018), as black circles, and of NGC 2419, the blue triangle.
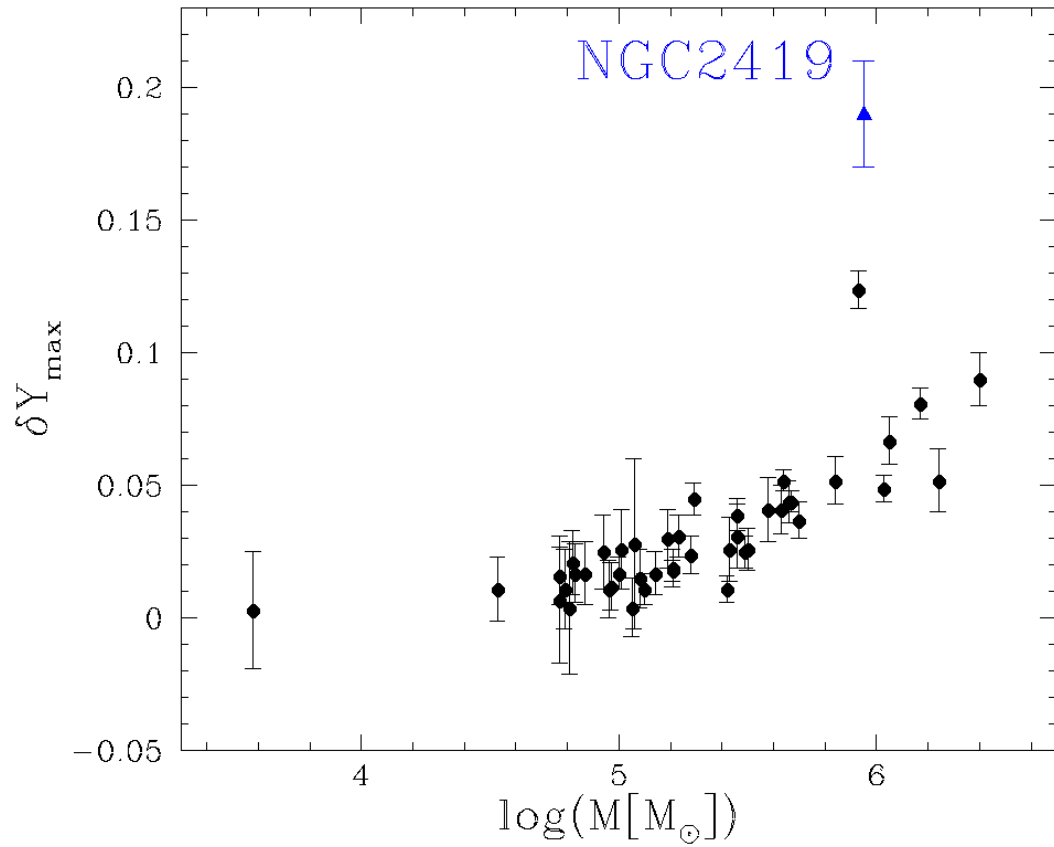
From their analysis they found that there is no significant correlation between the intrinsic RGB width and most of the global parameters, but a strong correlation, with a coefficient $r = 0.79 \pm 0.05$, exists between the $C_{F275W,F336W,F438W}$ RGB width and metallicity. They concluded that this relation was to be expected since at low metallicity the RGB colors become almost insensitive to metal abundances while the RGB-color sensitivity to composition increases with increasing metallicity.

In Fig. 4.7 I report the plot of the same clusters and $C_{F275W,F336W,F438W}$ RGB widths against the [Fe/H] with the addition of NGC 2419 as the usual blue triangle. From this image it is possible to see that NGC 2419 is located somewhat above from what would be expected by the relation found by Milone and collaborators, showing an higher value of the RGB width value for its metallicity. Still, this might not prove by itself that the relation previously observed is non-existing, since the width of the RGB of NGC 2419 was derived with not ideal data thus being subject to large errors. Furthermore this particular cluster could very well just be anomalous with respect to other clusters of the same metallicity.
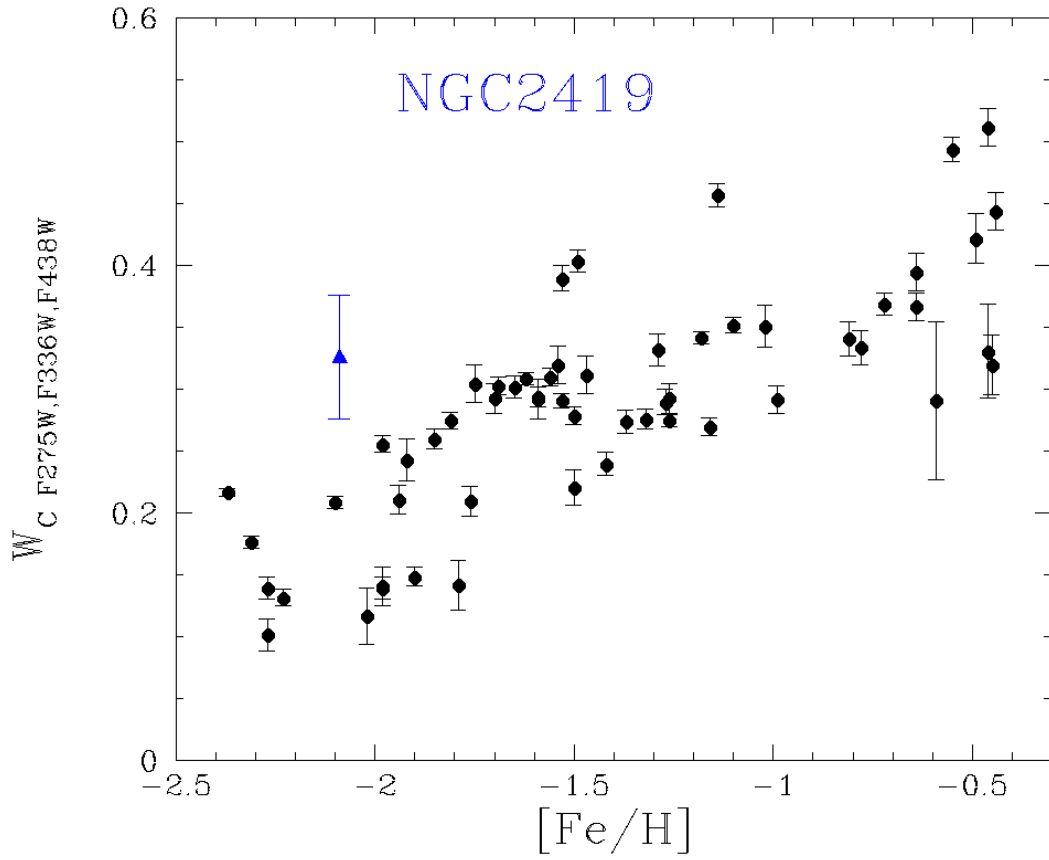
Figure 4.7: RGB widths vs. metallicity for the 57 GCs from Milone et al. (2016), represented by black circles and NGC 2419 represented by the blue triangle.

References

[1] Anderson, J. & Bedin, L. R. (2010). An Empirical Pixel-Based Correction for Imperfect CTE. I. HST Advanced Camera for Surveys. *pasp*, 122, 1035.

[2] Anderson, J. & King, I. R. (2000). Toward High-Precision Astrometry with WFPC2. I. Deriving an Accurate Point-Spread Function. *PASP*, 112, 1360–1382.

[3] Anderson, J., King, I. R., Richer, H. B., Fahlman, G. G., Hansen, B. M. S., Hurley, J., Kalirai, J. S., Rich, R. M., & Stetson, P. B. (2008). Deep Advanced Camera for Surveys Imaging in the Globular Cluster NGC 6397: Reduction Methods. *AJ*, 135, 2114–2128.

[4] Bastian, N., Lamers, H. J. G. L. M., de Mink, S. E., Longmore, S. N., Goodwin, S. P., & Gieles, M. (2013). Early disc accretion as the origin of abundance anomalies in globular clusters. *MNRAS*, 436, 2398–2411.

[5] Bastian, N. & Lardo, C. (2018). Multiple Stellar Populations in Globular Clusters. *Annual Review of Astronomy and Astrophysics*, 56, 83–136.

[6] Baumgardt, H., Hilker, M., Sollima, A., & Bellini, A. (2019). Mean proper motions, space orbits, and velocity dispersion profiles of Galactic globular clusters derived from Gaia DR2 data. *MNRAS*, 482, 5138–5155.

[7] Beccari, G., Bellazzini, M., Lardo, C., Bragaglia, A., Carretta, E., Dalessandro, E., Mucciarelli, A., & Pancino, E. (2013). Evidence for multiple populations in the massive globular cluster NGC 2419 from deep uVI LBT photometry. *MNRAS*, 431, 1995–2005.

[8] Bedin, L. (2009). Exploring the Bottom End of the White Dwarf Cooling Sequence in the Open Cluster NGC6819. HST Proposal.

[9] Bell, R. A. & Dickens, R. J. (1980). Chemical abundances in the globular clusters M3, M13, and NGC 6752. *ApJ*, 242, 657–672.

[10] Bellini, A., Anderson, J., Bedin, L. R., King, I. R., van der Marel, R. P., Piotto, G., & Cool, A. (2017). The State-of-the-art HST Astro-photometric Analysis of the Core of ω Centauri. I. The Catalog. *ApJ*, 842, 6.

[11] Campbell, S. W., D'Orazi, V., Yong, D., Constantino, T. N., Lattanzio, J. C., Stancliffe, R. J., Angelou, G. C., Wylie-de Boer, E. C., & Grundahl, F. (2013). Sodium content as a predictor of the advanced evolution of globular cluster stars. *Nature*, 498, 198–200.

[12] Cannon, R. D., Croke, B. F. W., Bell, R. A., Hesser, J. E., & Stathakis, R. A. (1998). Carbon and nitrogen abundance variations on the main sequence of 47 Tucanae. *MNRAS*, 298, 601–624.

[13] Carretta, E., Bragaglia, A., Gratton, R. G., Recio-Blanco, A., Lucatello, S., D'Orazi, V., & Cassisi, S. (2010). Properties of stellar generations in globular clusters and relations with global parameters. *A&A*, 516, A55.

[14] Castelli, F. (2005). ATLAS12: how to use it. *Memorie della Societa Astronomica Italiana Supplementi*, 8, 25.

[15] Chantereau, W., Charbonnel, C., & Meynet, G. (2016). Evolution of long-lived globular cluster stars. III. Effect of the initial helium spread on the position of stars in a synthetic Hertzsprung-Russell diagram. *A&A*, 592, A111.

[16] Cohen, J. G., Huang, W., & Kirby, E. N. (2011). The Peculiar Chemical Inventory of NGC 2419: An Extreme Outer Halo "Globular Cluster". *ApJ*, 740, 60.

[17] Cohen, J. G. & Kirby, E. N. (2012). The Bizarre Chemical Inventory of NGC 2419, An Extreme Outer Halo Globular Cluster. *ApJ*, 760, 86.

[18] D'Antona, F., Caloi, V., Montalbán, J., Ventura, P., & Gratton, R. (2002). Helium variation due to self-pollution among Globular Cluster stars. Consequences on the horizontal branch morphology. *A&A*, 395, 69–75.

[19] Dantona, F., Gratton, R., & Chieffi, A. (1983). CNO self-pollution in globular clusters - A model and its possible observational tests. *Mem. Soc. Astron. Ital.*, 54, 173–198.

[20] D'Antona, F., Vesperini, E., D'Ercole, A., Ventura, P., Milone, A. P., Marino, A. F., & Tailo, M. (2016). A single model for the variety of multiple-population formation(s) in globular clusters: a temporal sequence. *MNRAS*, 458, 2122–2139.

[21] de Mink, S. E., Pols, O. R., Langer, N., & Izzard, R. G. (2009). Massive binaries as the source of abundance anomalies in globular clusters. *A&A*, 507, L1–L4.

[22] Decressin, T., Meynet, G., Charbonnel, C., Prantzos, N., & Ekström, S. (2007). Fast rotating massive stars and the origin of the abundance patterns in galactic globular clusters. *A&A*, 464, 1029–1044.

[23] Denisenkov, P. A. & Denisenkova, S. N. (1990). Correlation Between the Abundances of NA and the CNO Elements in Red Giants in Omega-Centauri. *Soviet Astronomy Letters*, 16, 275.

[24] Denissenkov, P. A. & Hartwick, F. D. A. (2014). Supermassive stars as a source of abundance anomalies of proton-capture elements in globular clusters. *MNRAS*, 437, L21–L25.

[25] Denissenkov, P. A., VandenBerg, D. A., Hartwick, F. D. A., Herwig, F., Weiss, A., & Paxton, B. (2015). The primordial and evolutionary abundance variations in globular-cluster stars: a problem with two unknowns. *MNRAS*, 448, 3314–3324.

[26] D'Ercole, A., D'Antona, F., Ventura, P., Vesperini, E., & McMillan, S. L. W. (2010). Abundance patterns of multiple populations in globular clusters: a chemical evolution model based on yields from AGB ejecta. *MNRAS*, 407, 854–869.

[27] D'Ercole, A., Vesperini, E., D'Antona, F., McMillan, S. L. W., & Recchi, S. (2008). Formation and dynamical evolution of multiple stellar generations in globular clusters. *MNRAS*, 391, 825–843.

[28] di Criscienzo, M., D'Antona, F., Milone, A. P., Ventura, P., Caloi, V., Carini, R., D'Ercole, A., Vesperini, E., & Piotto, G. (2011). NGC 2419: a large and extreme second generation in a currently undisturbed cluster. *MNRAS*, 414, 3381–3393.

[29] Di Criscienzo, M., Greco, C., Ripepi, V., Clementini, G., Dall'Ora, M., Marconi, M., Musella, I., Federici, L., & Di Fabrizio, L. (2011). A New Census of the Variable Star Population in the Globular Cluster NGC 2419. *AJ*, 141, 81.

[30] Dotter, A., Chaboyer, B., Jevremović, D., Kostov, V., Baron, E., & Ferguson, J. W. (2008). The Dartmouth Stellar Evolution Database. *ApJS*, 178, 89–101.

[31] Dotter, A., Sarajedini, A., Anderson, J., Aparicio, A., Bedin, L. R., Chaboyer, B., Majewski, S., Marín-Franch, A., Milone, A., Paust, N., Piotto, G., Reid, I. N.,

Rosenberg, A., & Siegel, M. (2010). The ACS Survey of Galactic Globular Clusters. IX. Horizontal Branch Morphology and the Second Parameter Phenomenon. *ApJ*, 708, 698–716.

[32] Harris, W. E. (1996). A Catalog of Parameters for Globular Clusters in the Milky Way. *AJ*, 112, 1487.

[33] Iben, I. & Renzini, A. (1984). Single star evolution I. Massive stars and early evolution of low and intermediate mass stars. *Phys. Rep.*, 105, 329–406.

[34] Karakas, A. I., Marino, A. F., & Nataf, D. M. (2014). Nucleosynthesis in Helium-enriched Asymptotic Giant Branch Models: Implications for Heavy Element Enrichment in ω Centauri. *ApJ*, 784, 32.

[35] Krause, M., Charbonnel, C., Decressin, T., Meynet, G., & Prantzos, N. (2013). Superbubble dynamics in globular cluster infancy. II. Consequences for secondary star formation in the context of self-enrichment via fast-rotating massive stars. *A&A*, 552, A121.

[36] Kurucz, R. L. (2005). ATLAS12, SYNTHE, ATLAS9, WIDTH9, et cetera. *Memorie della Societa Astronomica Italiana Supplementi*, 8, 14.

[37] Lapenna, E., Lardo, C., Mucciarelli, A., Salaris, M., Ferraro, F. R., Lanzoni, B., Massari, D., Stetson, P. B., Cassisi, S., & Savino, A. (2016). Lost and Found: Evidence of Second-generation Stars Along the Asymptotic Giant Branch of the Globular Cluster NGC 6752. *ApJL*, 826, L1.

[38] Lee, Y.-W., Han, S.-I., Joo, S.-J., Jang, S., Na, C., Okamoto, S., Arimoto, N., Lim, D., Kim, H.-S., & Yoon, S.-J. (2013). Two Distinct Red Giant Branch Populations in the Globular Cluster NGC 2419 as Tracers of a Merger Event in the Milky Way*. *ApJ*, 778, L13.

[39] Marino, A. F., Milone, A. P., Yong, D., Da Costa, G., Asplund, M., Bedin, L. R., Jerjen, H., Nardiello, D., Piotto, G., Renzini, A., & Shetrone, M. (2017). Spectroscopy and Photometry of Multiple Populations along the Asymptotic Giant Branch of NGC 2808 and NGC 6121 (M4). *ApJ*, 843, 66.

[40] Marino, A. F., Sneden, C., Kraft, R. P., Wallerstein, G., Norris, J. E., Da Costa, G., Milone, A. P., Ivans, I. I., Gonzalez, G., Fulbright, J. P., Hilker, M., Piotto, G., Zoccali, M., & Stetson, P. B. (2011). The two metallicity groups of the globular cluster M 22: a chemical perspective. *A&A*, 532, A8.

[41] Marino, A. F., Villanova, S., Piotto, G., Milone, A. P., Momany, Y., Bedin, L. R., & Medling, A. M. (2008). Spectroscopic and photometric evidence of two stellar populations in the Galactic globular cluster NGC 6121 (M 4). *A&A*, 490, 625–640.

[42] McLaughlin, D. E. & van der Marel, R. P. (2005). Resolved Massive Star Clusters in the Milky Way and Its Satellites: Brightness Profiles and a Catalog of Fundamental Parameters. *ApJS*, 161, 304–360.

[43] Milone, A. P. (2015). Helium and multiple populations in the massive globular cluster NGC 6266 (M 62). *MNRAS*, 446, 1672–1684.

[44] Milone, A. P., Marino, A. F., Bedin, L. R., Anderson, J., Apai, D., Bellini, A., Bergeron, P., Burgasser, A. J., Dotter, A., & Rees, J. M. (2017a). The HST large programme on ω Centauri - I. Multiple stellar populations at the bottom of the main sequence probed in NIR-Optical. *MNRAS*, 469, 800–812.

[45] Milone, A. P., Marino, A. F., Renzini, A., D'Antona, F., Anderson, J., Barbuy, B., Bedin, L. R., Bellini, A., Brown, T. M., Cassisi, S., Cordoni, G., Lagioia, E. P., Nardiello, D., Ortolani, S., Piotto, G., Sarajedini, A., Tailo, M., van der Marel, R. P., & Vesperini, E. (2018). The Hubble Space Telescope UV legacy survey of galactic globular clusters - XVI. The helium abundance of multiple populations. *MNRAS*, 481, 5098–5122.

[46] Milone, A. P., Piotto, G., Bedin, L. R., Cassisi, S., Anderson, J., Marino, A. F., Pietrinferni, A., & Aparicio, A. (2012). Luminosity and mass functions of the three main sequences of the globular cluster NGC 2808. *A&A*, 537, A77.

[47] Milone, A. P., Piotto, G., Renzini, A., Marino, A. F., Bedin, L. R., Vesperini, E., D'Antona, F., Nardiello, D., Anderson, J., King, I. R., Yong, D., Bellini, A., Aparicio, A., Barbuy, B., Brown, T. M., Cassisi, S., Ortolani, S., Salaris, M., Sarajedini, A., & van der Marel, R. P. (2017b). The Hubble Space Telescope UV Legacy Survey of Galactic globular clusters - IX. The Atlas of multiple stellar populations. *MNRAS*, 464, 3636–3656.

[48] Mucciarelli, A., Bellazzini, M., Ibata, R., Merle, T., Chapman, S. C., Dalessandro, E., & Sollima, A. (2012). News from the Galactic suburbia: the chemical composition of the remote globular cluster NGC 2419. *MNRAS*, 426, 2889–2900.

[49] Nardiello, D., Milone, A. P., Piotto, G., Anderson, J., Bedin, L. R., Bellini, A., Cassisi, S., Libralato, M., & Marino, A. F. (2018). The Hubble Space Telescope UV

Legacy Survey of Galactic globular clusters - XIV. Multiple stellar populations within M 15 and their radial distribution. *MNRAS*, 477, 2004–2019.

[50] Osborn, W. (1971). Two new CN-strong globular cluster stars. *The Observatory*, 91, 223–224.

[51] Renzini, A. (1983). Current problems in the interpretation of the characteristics of globular clusters. *Mem. Soc. Astron. Ital.*, 54, 335–354.

[52] Renzini, A., D'Antona, F., Cassisi, S., King, I. R., Milone, A. P., Ventura, P., Anderson, J., Bedin, L. R., Bellini, A., Brown, T. M., Piotto, G., van der Marel, R. P., Barbuy, B., Dalessandro, E., Hidalgo, S., Marino, A. F., Ortolani, S., Salaris, M., & Sarajedini, A. (2015). The Hubble Space TelescopeUV Legacy Survey of Galactic Globular Clusters - V. Constraints on formation scenarios. *MNRAS*, 454, 4197–4207.

[53] Sabbi, E., Lennon, D. J., Anderson, J., Cignoni, M., van der Marel, R. P., Zaritsky, D., De Marchi, G., Panagia, N., Gouliermis, D. A., Grebel, E. K., Gallagher, III, J. S., Smith, L. J., Sana, H., Aloisi, A., Tosi, M., Evans, C. J., Arab, H., Boyer, M., de Mink, S. E., Gordon, K., Koekemoer, A. M., Larsen, S. S., Ryon, J. E., & Zeidler, P. (2016). Hubble Tarantula Treasury Project. III. Photometric Catalog and Resulting Constraints on the Progression of Star Formation in the 30 Doradus Region. *ApJS*, 222, 11.

[54] Sbordone, L., Bonifacio, P., & Castelli, F. (2007). ATLAS 9 and ATLAS 12 under GNU-Linux. In F. Kupka, I. Roxburgh, & K. L. Chan (Eds.), *Convection in Astrophysics*, volume 239 of *IAU Symposium* (pp. 71–73).

[55] Sneden, C., Kraft, R. P., Prosser, C. F., & Langer, G. E. (1992). Oxygen abundances in halo giants. III - Giants in the mildly metal-poor globular cluster M5. *AJ*, 104, 2121–2140.

[56] Tailo, M., D'Antona, F., Vesperini, E., di Criscienzo, M., Ventura, P., Milone, A. P., Bellini, A., Dotter, A., Decressin, T., D'Ercole, A., Caloi, V., & Capuzzo-Dolcetta, R. (2015). Rapidly rotating second-generation progenitors for the 'blue hook' stars of ω Centauri. *Nature*, 523, 318–321.

[57] Ventura, P., D'Antona, F., Mazzitelli, I., & Gratton, R. (2001). Predictions for Self-Pollution in Globular Cluster Stars. *ApJL*, 550, L65–L69.

[58] Villanova, S., Piotto, G., & Gratton, R. G. (2009). The helium content of globular clusters: light element abundance correlations and HB morphology. I. NGC 6752. *A&A*, 499, 755–763.

[59] Wang, Y., Primas, F., Charbonnel, C., Van der Swaelmen, M., Bono, G., Chantereau, W., & Zhao, G. (2016). Sodium abundances of AGB and RGB stars in Galactic globular clusters. I. Analysis and results of NGC 2808. *A&A*, 592, A66.

[60] Yong, D., Grundahl, F., Johnson, J. A., & Asplund, M. (2008). Nitrogen Abundances in Giant Stars of the Globular Cluster NGC 6752. *ApJ*, 684, 1159–1169.